AN ABSTRACT OF THE THESIS OF

Douglas C. Snell for the degree of Doctor of Philosophy in Mechanical Engineering presented on June 2, 1994.

Title: A Study of a Diffusionally Controlled Reactive Synthesis Process Using a Multi-tube Diffusion Flame Burner

Abstract approved: Redacted for Privacy

Richard B. Peterson

A continuous process for the production of ceramic materials has been studied. This method reacted metal and oxidizer in a diffusionally controlled process, demonstrated by reacting a magnesium particle stream and hot water vapor. Many small rich hydrogen/air diffusion flames provide an atmosphere of hot water vapor, hydrogen, and nitrogen for oxidizing the magnesium, which reacts with the water vapor in the form of a diffusion flame. The burner that provides the hot atmosphere has been characterized thermally using thermocouple measurements and a model that gives the true temperature from the measured values. A model was developed that gives the flame profile for the parallel flow geometry of particle stream combustion used in this study as defined in the cartesian coordinate system.

A Study of a Diffusionally Controlled Reactive Synthesis Process using a Multi-tube Diffusion Flame Burner

by

Douglas C. Snell

A THESIS

Submitted to

Oregon State University

In partial fulfillment of the

requirements for the degree of

Doctor of Philosophy

Completed June 2, 1994

Commencement June, 1995

APPROVED:

Redacted for Privacy

Associate Professor of Mechanical Engineering in charge of major

Redacted for Privacy

Head of Department of Mechanical Engineering

Redacted for Privacy

Dean of Graduate School

Date thesis is presented June 2, 1994

Typed by researcher for Douglas C. Snell

ACKNOWLEDGEMENT

When I left California State University, Chico to pursue graduate education Dr. Dennis Blackketter bequeathed me with this bit of truth, "When you set out to earn a Ph.D. your primary goal is to learn as much as you possibly can. Your second goal is to get out as fast as you can. If you accomplish the latter, you will fulfill the former." Four years and nine months later...well, one out of two isn't bad. Along the way, I have received much help and support.

I would like to thank my advisor, Dr. Richard Peterson, for the research idea and his guidance during the research process. Thank you as well to those professors willing to serve on my committee, Dr. Jim Welty, Dr. Mike Kassner, and Dr. Alan Hernried.

Earning a Ph.D. requires more than intellectual support and my friends at school, Heidi Pattee, Joe Zaworski, Tim Weber, and Dave Pidwerbecki, and my friends at Faith Lutheran Church, especially Nick and Kris Doversberger, have provided emotional and spiritual stability during this journey.

Most of all, thank you to my family for coming along for the ride and making it so much more enjoyable! Thank you to Becca, who wonders what I do at my school, to Sara, who loves trips to the candy machine for a bag of Skittles, to Matthias, who always welcomes me home with much enthusiasm if he is not too busy rolling up potato bugs, and to my loving wife Kathryn, who I now may be able to keep in the manner to which she would like to become accustomed.

TABLE OF CONTENTS

Chapter	Page
1. INTRODUCTION	1
1.1 Overview	1
1.2 Background	2
1.3 Organization	5
2. BURNER AND PARTICLE FORMATION CHAMBER	7
2.1 Burner Design	8
2.2 Particle Formation Chamber	11
3. BURNER CHARACTERIZATION	16
3.1 Experimental Procedure	16
3.2 Thermocouple Model	20
3.3 Profiles	26
3.4 Shapes and Heights of the Flames	31
3.5 Uncertainty Analysis	34
3.6 Improvements in the Burner	37
4. PARTICLE STREAM DIFFUSION FLAME MODEL	39
4.1 Flame Model	39
4.2 Cartesian Coordinate System	43
4.3 Cylindrical Coordinate System	51
4.4 Model Results for the Cartesian Coordinate System	56
5. MAGNESIUM-WATER VAPOR REACTION PROFILE	61
5.1 Experimental Procedure	61
5.2 Reaction Profile Appearance	65
5.3 Results	67
6. MAGNESIUM-WATER VAPOR TEMPERATURE PROFILE	70
6.1 Experimental Procedure	70
6.2 Temperature Profile	71
6.3 Magnesium Oxidation	73
7. CONCLUSION	79
7.1 Accomplishments	79
7.2 Further Study	79

TABLE OF CONTENTS (CONTINUED)

Chapter	Page
BIBLIOGRAPHY	81
APPENDIX	85

LIST OF FIGURES

Figure		Page
Figure 1.	Profile view of burner with inset showing tube pattern.	9
Figure 2.	Particle Formation Chamber	12
Figure 3.	Magnesium Particle Size Photograph	15
Figure 4.	Geometric tube arrangement with horizontal and vertical lines of probing. Thermocouple shown in the L-shaped configuration for measuring the temperature profile over the tubes.	19
Figure 5.	Concentric rings used to generate environment temperature profile for use in model.	27
Figure 6.	Temperature profiles for $\phi = 0.5$	28
Figure 7.	Temperature profiles for $\phi = 1$	29
Figure 8.	Temperature profiles for $\phi = 2$	30
Figure 9.	Model Geometry	40
Figure 10.	Coordinate Systems: (a) Cartesian and (b) Cylindrical	41
Figure 11.	Flame Model Profiles: Variation with $v_o d^2/D_o$	57
Figure 12.	Flame Model Profiles: Variation with Particle to Oxidizer Ratio	58
Figure 13.	Dimensionless Flame Height vs. Φ_D	60
Figure 14.	Experimental Magnesium/Water Vapor Reaction Profiles	66
Figure 15.	Sequence of Video Frames Showing Instability of Reaction Profile	68
Figure 16.	Measured Profile of Magnesium/Water Vapor Reaction	69

LIST OF FIGURES (CONTINUED)

Figure	Page
Figure 17. Temperature Profile with Magnesium/Water Vapor Reaction	74
Figure 18. Ignition Temperature for Single Magnesium Particles (from Cassel and Liebman, 1959)	76

LIST OF TABLES

Table	Page
I. Properties of Magnesium	15
II. Values of λ as a function of Φ_D	51

NOMENCLATURE

a = particle radius

A = area; constant of integration

B = constant of integration

C = celsius; concentration

d = supply tube width; flame width

D = diffusion coefficient

erf = error function

erfc = compliment error function

f = mass ratio of fuel to oxidizer

h = convective heat transfer coefficient

H = flame height

k = thermal conductivity, Boltzmann's constant

M = molecular weight

n = moles

n = molar flow rate

P = pressure

r = cylindrical coordinate

R = radius of flame

R = universal gas constant

t = time

T = temperature

V = volts; volume

V = volume flow rate

x = cartesian coordinate

X = flame half-width

y = cartesian and cylindrical coordinate

Greek

Δ = delta

ϵ = emissivity

η = similarity variable

λ = constant for model analysis

Φ_D = ratio of supply mass ratio to stoichiometric mass ratio, f_{supp}/f_{st}

σ = Stefan-Boltzmann constant for radiation

θ = dimensionless concentration profile, $C_o/C_{o,\infty}$

υ = velocity

ν = viscosity

Superscripts

° = degree

′ = denotes cylindrical coordinate system

Subscripts

bead = thermocouple bead

D = diffusion

f = fuel

H2O = H_2O

ij = parts of the molecule j

ini = initial or supply

m = arbitrary node location

n = last node location

o = oxidizer

st = stoichiometric

supp = supply

sur = local surroundings

wire = thermocouple wire

0,1,2 = node numbers, molecular species

0,old = previous iteration values at node location zero

∞ = ambient surroundings; freestream conditions

A STUDY OF A DIFFUSIONALLY CONTROLLED REACTIVE SYNTHESIS PROCESS USING A MULTI-TUBE DIFFUSION FLAME BURNER

1. INTRODUCTION

1.1 Overview

Synthesis is the intentional formation of a substance from its elemental components or from molecules containing those elements. A new material can be synthesized by various means, but one of the most common methods is to react two substances. For example, titanium carbide is often synthesized from the reaction of titanium with carbon. Synthesis can occur between all forms of matter - solid, liquid and vapor.

The goal of this work is to study a diffusionally controlled reactive synthesis process to produce a ceramic material. The choice of this method for producing ceramics is motivated by the economic advantage of continuous production over batch production. Currently, many ceramics are manufactured one batch at a time, which by nature is slow and costly. The reactive synthesis process studied has the potential to be continuous.

The method was demonstrated by reacting magnesium with hot water vapor to form magnesium oxide (MgO). MgO can be produced easily by other means, but it is the study of the process that is the thrust of this investigation, not the production of a particular ceramic.

Essentially, the technique involved producing a magnesium particle flow and combining it with water vapor in a hot environment. The magnesium flow was generated by vaporizing the metal with a D.C. arc in the presence of argon. The resulting particulate flow was carried into a reactive atmosphere of hot hydrogen, nitrogen, and water vapor produced by many small diffusion flames of hydrogen and air. The water vapor adjacent to the magnesium flow was consumed by reaction with the magnesium and replenished by water vapor diffusing through the reactive atmosphere. Since the rate of reaction was very fast compared to the rate of diffusion the process was diffusionally controlled. However, unlike typical raindrop-shaped diffusion flames such as pilot lights and candles, the reaction boundary was shaped like a finger.

1.2 Background

The past twenty years have seen a dramatic increase in the use and value of ceramic materials. From the substrate of computer chips to the tiles of the space shuttle, ceramics are finding increased usage due to their thermal properties and ability to resist wear. In the case of integrated circuits beryllium oxide (BeO) and now aluminum nitride (AlN) are used as substrate material because of their high thermal conductivity, low coefficient of expansion, and extremely high resistance to the conduction of electricity (Shaffer et al., 1989). Many of these properties, however, depend on the purity of the ceramic which in turn is dependent on its method of production (Shaffer et al., 1989).

Many methods have been devised for producing ceramics. For developing thin films of ceramic material, methods include chemical vapor deposition processes (Yoshida

et al., 1975; Bauer et al., 1977; Nickel et al., 1989, Demiryont et al., 1986), plasma techniques (Bauer et al., 1977; Meikle et al., 1990) and reactive molecular beam epitaxy (Yoshida et al., 1979). While these deposition methods are useful for the manufacture of integrated circuits and similar devices, they do not lend themselves to large scale production of ceramics. For the mass production of ceramics, manufacturers turn to processes like solid phase combustion synthesis (Hlavacek, 1991; Miyamoto, 1990), carbothermal reduction (Shaffer et al, 1989; Sohn and Harbuck, 1986) and flame synthesis (Ulrich, 1984).

In solid phase combustion synthesis, one or more of the components are in the form of fine powder. The ingredients are well-mixed and in the case of a gaseous ingredient this is ensured by pressurizing the powder with the gas. The mixture is placed in a mold and heated at one end until the components react. The reaction propagates through the mixture, leaving a ceramic shaped like the mold. Another common production technique is carbothermal reduction, used to produce aluminum nitride from aluminum oxide. Crushed aluminum oxide is heated and exposed to a carbon source and nitrogen gas at high pressures. The aluminum oxide is reduced by the carbon, leaving the aluminum to react with the nitrogen to form AlN. Both solid phase combustion synthesis and carbothermal reduction, like many methods for producing ceramics, are batch processes.

A contrasting approach is the concept of continuous production, which can occur as long as the components of the product are supplied to the reaction site. Flow synthesis techniques fall into this category. In reactive flow processes, the ceramic is

formed as its components come together in a hot environment. One example of this method are current flame synthesis techniques that use a flame to burn a molecule containing metal. For example, titanium dioxide, a common whitener for paint, is routinely produced by burning titanium tetrachloride (Ulrich, 1984). These methods, however, can produce noxious byproducts such as chlorine. In addition, there may be little control over the chemical composition of the oxidizing environment.

The synthesis method studied here is a reactive flow process differing from current flame strategies because the metal is supplied in its pure form as particles. Also, rather than flow with the fuel or oxidizer into a flame, the particle stream and oxidizer flows are separate and parallel. With this configuration particles and oxidizer are brought together by diffusion. As the metal and oxidizer first come into contact with each other they react to form a product. This depletes the concentration of the reactants at the reaction zone so more of each species diffuses toward the depleted region. The diffusing oxider and metal react and the process continues until the particles are completely consumed. This method is diffusion controlled or diffusion-limited because the reactants combine as fast as they diffuse into each other. The particle and oxidizer form a distinct reaction boundary like that found with common gas diffusion flames such as candles and pilot lights.

The advantage of diffusion controlled synthesis is the capability to control the reactive process by varying the particle flow rate and reactive atmosphere. In addition, since the particles and gaseous component react at a distinct location it is possible to observe and investigate the influences of these changes.

1.3 Organization

To take advantage of the diffusion-limited reaction profile, a well characterized and stable experimental system had to be developed. This was accomplished by design and construction of an experiment consisting of a particle formation chamber and a multitube diffusion flame burner. This configuration allowed precise control of temperature and chemical composition of the reactive environment. Chapter 2 describes the burner and particle formation chamber and how they operate in relation to one another.

In order to characterize the thermal environment of the burner, temperature measurements were made for three hydrogen-to-air supply ratios. Chapter 3 describes the experimental technique for the measurements and a model that was used to determine actual gas temperatures from measured values. A comparison of the shapes and heights of the individual diffusion flames with theory is also offered.

Although much attention has been given to modeling gas diffusion-limited flames (Burke and Schumann, 1928; Roper, 1977a, 1977b, 1979) modeling has not been done for a particle/gas diffusion controlled flame. Chapter 4 gives the derivation of a model for the shape of a diffusion-limited particle flame in cartesian coordinates. A derivation for cylindrical coordinates was also attempted, but was unsuccessful. Since this latter geometry is that of the actual reaction profile no exact comparison between model and experiment was possible. However, Chap. 5 does give a description of the magnesium/water vapor reaction profile as well as a plot of its contour.

Measurements of the thermal environment near a diffusion-limited reaction can yield information about the reaction. Chapter 6 describes the experimental technique used to obtain a horizontal temperature profile that passes through the reaction boundary. The true gas temperatures were obtained using the same model that was employed in Chap. 3. The measurements indicate negligible heat release from the magnesium/water vapor reaction. The ignition and oxidation of the particles is discussed in light of this observation. Note that because the process does not appear to be exothermic the reaction profile will not be referred to as a flame.

Chapter 7 summarizes the accomplishments of this study and suggests opportunities for further study.

2. BURNER AND PARTICLE FORMATION CHAMBER

Since the best thermal and chemical conditions for oxidizing the magnesium particles were not known prior to the experiment, a burner was needed that would provide reactive atmospheres over a wide range of temperatures and compositions. Essentially there are two kinds of burners; mixed reactant and diffusion. In mixed reactant or pre-mixed burners, the reactants flow together into the flame. With this system the flammability limits are confined to those of the mixture with minor influences from the burner because of heat loss. Furthermore, these burners can be unsafe because the flame can propagate upstream against the reactant flow, causing flashback. In diffusion flame burners, the fuel and oxidizer flows are separate and parallel to each other, and the reactants are brought together at stoichiometric ratio by diffusion. This condition holds regardless of the supply ratio of fuel and oxidizer, which gives diffusion burners much wider flammability limits than their pre-mixed counterparts. Also, flashback is not a problem since the flame cannot travel down the separate supply lines. With these advantages as well as the ability to widely vary the flow rates of the fuel and oxidizer, a unique diffusion burner was built for this work.

Most of the diffusion burners that exist today have been developed for flame diagnostics (Fristrom and Westenberg, 1965). Very few have been designed to serve as the heat source for a secondary combustion process. One example of a burner designed for the combustion of metal powder is that given by Fassel et al, 1960. They designed two "metal powder torches" for burning large (25 μm) particles of aluminum and

magnesium, but the torches were not designed to provide fine control of the temperature, flow, or composition of the oxidizing environment. For diagnostic work, Krupa et al., 1986, described a multi-tube diffusion flame burner that was shielded. A unique feature of the burner was the three reactant zone configuration. Only oxidizer and the atomized sample were permitted in the center tube assembly thus isolating the sample from the surrounding air. Other flame diagnostic burners can be found in a review of the subject (Schrenk, 1986).

The burner developed for this work is similar to a design used to study the combustion of fuel samples (Hencken, 1994). Both burners use many small diffusion flames to provide a hot, uncontaminated environment for combustion. The temperature and composition in the post flame gases are easily controlled by varying the flow rates of the primary fuel and oxidizer. A central tube through the burner is used to transport a sample flow to the hot environment created by the multiple diffusion flames. The principle differences between the burners are the fuel and sample flow tube sizes. The fuel tubes for the reaction synthesis burner have twice the diameter of the "Hencken burner" and the sample flow tube is approximately seven times as large. In addition, the "Hencken burner" provides for an inert coaxial flow around the periphery of the burner that works as a shield for the fuel/oxidizer flows.

2.1 Burner Design

The burner shown in Fig. 1 consists of a stainless steel housing, a quartz tube bundle, and a center brass tube. The housing is fashioned from two pieces of stainless

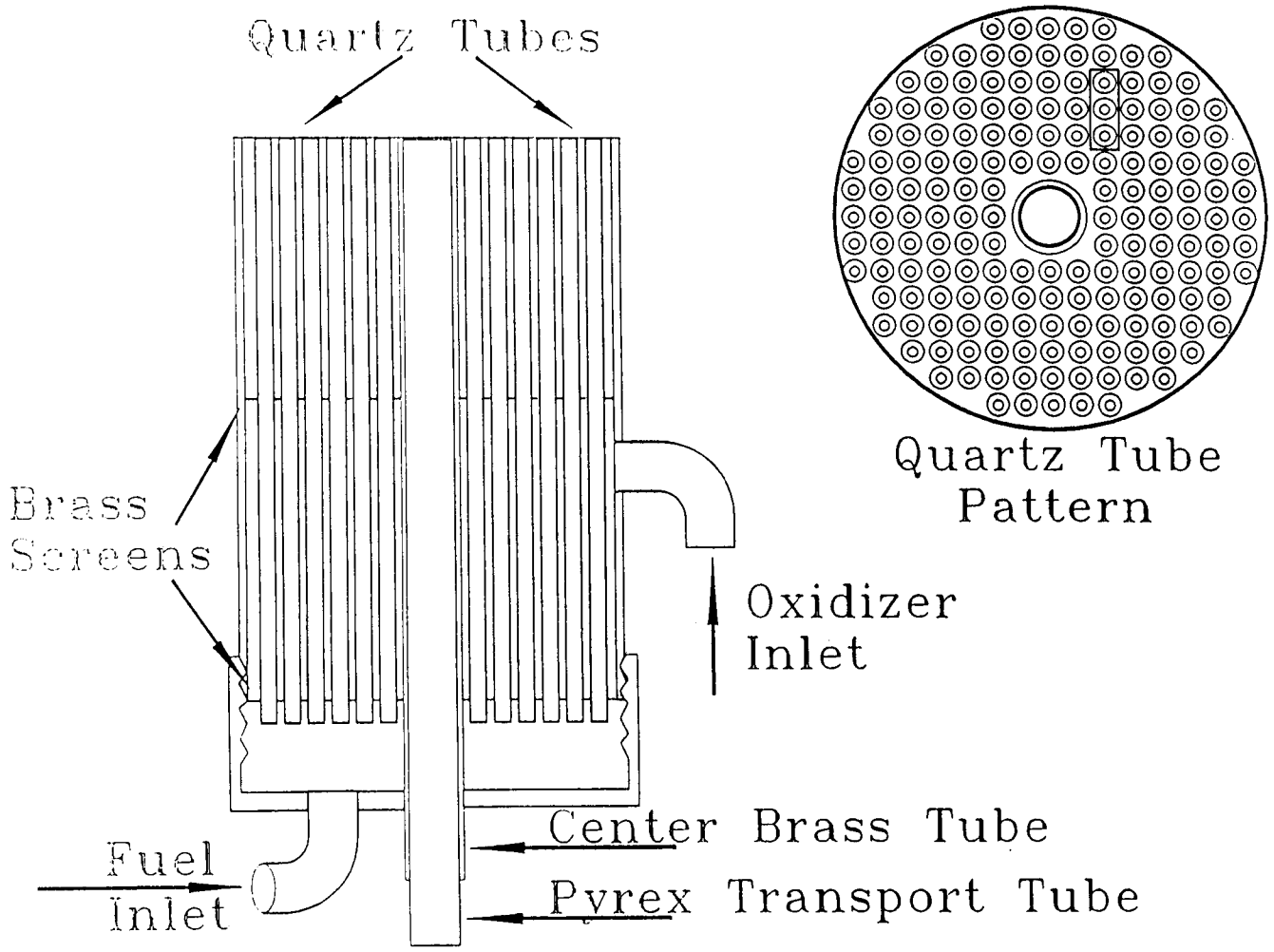

Figure 1. Profile view of burner with inset showing tube pattern.

steel (type 304) pipe; a nipple 10 cm long by 5 cm in diameter is the cylindrical wall of the burner, and an end cap 2.5 cm long is used for the bottom of the burner. Both pieces have wall thicknesses of approximately 6.4 mm and are screwed together to form the housing. Note that the nipple has had the threads machined from one end. This facilitates the attachment of a copper cooling coil to the top of the burner.

The tube bundle is an array of 10.5 cm long quartz tubes supported by two perforated sheets. The perforations have a 3.3 mm square grid pattern of 2 mm diameter holes. The quartz tubes have inner and outer diameters of 1.0 mm and 1.5 mm, respectively. One of the perforated sheets is secured to the end of the cylindrical housing with a high temperature semi-flexible epoxy. Also, each quartz tube passing through the bottom sheet is sealed in place with the epoxy to prevent one gaseous reactant from mixing with the other. The upper brass screen provides spacing for the tube bundle and dispersal of the air flow (as explained below). The thin-walled brass tube located along the centerline of the burner has an inside diameter of 11.0 mm and is epoxied to the bottom of the burner housing and to both perforated sheets. The inset to Fig. 1 is a top view of the burner showing the center tube and the pattern of the surrounding tube bundle.

The lower perforated sheet separates the burner into two chambers. The lower chamber is completely enclosed having the screen and the pipe cap for its boundaries. The upper chamber is open at the top by way of the annular gap between each quartz tube and the perforation it passes through in the top sheet. The lower sheet, sealed with epoxy, acts as the lower wall for the upper chamber. The epoxy used to secure the tubes

and lower sheet serves as an effective seal for separating the two chambers. The oxidizer enters the upper chamber through a fitting in the side wall of the burner and is distributed through the small gaps between the perforations and tubes. Fuel enters the bottom chamber by way of another fitting located in the end cap and flows up through the quartz tubes where a flame is established over each individual tube.

2.2 Particle Formation Chamber

The particles are generated by vaporizing magnesium with an electric arc in a chamber purged with argon. The particles are then entrained in the argon flow and transported to the reaction zone. This method of particle formation was chosen for its ability to supply uniform dense flows of micron size particles that were slightly elevated in temperature. An elevated supply temperature aids the reaction process by decreasing the time for particle consumption. A uniform flow of particles is needed to provide a steady reaction boundary. Small particles are desired because they will take less time to oxidize. The volume and mass flow rates of the argon and magnesium and their method of determination are given in Chap. 5.

The particle formation chamber is located directly beneath the burner, Fig. 2. A one litre, thick-walled pyrex beaker forms the sides and bottom of the chamber and an aluminum ring is epoxied to the rim of the beaker. The top plate is an aluminum disk that has all the accesses to the chamber mounted in it. A rubber gasket between the ring and plate acts as a seal and the pieces are clamped together during operation.

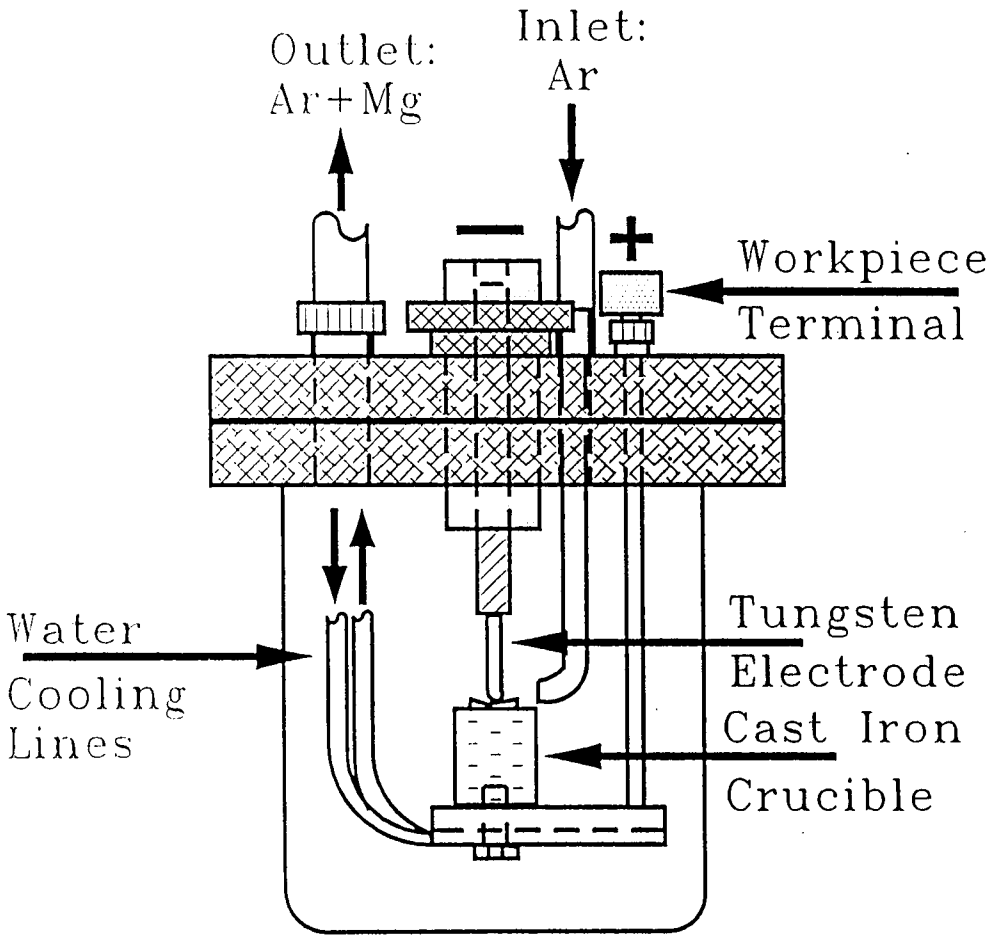

Figure 2. Particle Formation Chamber

The arc used to vaporize the magnesium is generated by a portable stick welder delivering 40 amps at 25 V DC. As indicated on Fig. 2 the center terminal serves as the negative junction with the actual electrode being a 3.2 mm dia. x 50 mm long tungsten rod. Approximately 10 mm of the tungsten rod is held inside the end of a 6.35 mm dia. allen-head bolt with a set screw. The allen-head bolt sets concentrically inside a 25.4 mm dia. x 59.3 mm brass cylinder that was drilled and tapped for the bolt. Turning the bolt adjusts the height of the electrode. The positive workpiece terminal is a 12.6 mm dia. x 15.4 mm cylinder of aluminum. The aluminum cylinder is machined in the center to fit the end of a 2.9 mm dia. brass rod that passes through the top aluminum plate and extends down into the chamber.

The brass rod is attached to a 31.3 x 72.6 x 9.8 mm thick piece of aluminum plate that serves as the mount for the crucible that holds the magnesium. A 1.6 mm copper water cooling line runs through the underside of the aluminum plate. The cooling line enters and exits the chamber through the top aluminum plate. The crucible is a 25.4 mm dia. x 31.4 mm cylinder machined out of cast iron. Cast iron was chosen because of its low reactivity with molten magnesium (Beck, 1940). The top of the crucible is slightly concave, to form a well for the magnesium, and the bottom is drilled and tapped for a 9.53 mm diameter bolt, which holds the crucible to the aluminum plate.

The argon blown into the chamber enters through a 4.6 mm dia. copper tube and is directed at the arc location. As the magnesium is vaporized the concentration of its vapor builds and the arc lengthens, sputters, and eventually extinguishes. It was not clear whether the arc extinguished because it became too long, the magnesium vapor

interfered with it, or a combination of both, but blowing the argon at the surface of the vaporizing magnesium increased the time before extinguishment, which typically was about two minutes. The magnesium becomes entrained in the argon flow and exits the chamber into a transport tube that leads to the burner.

The transport tube is divided into three sections. The bottom and top sections are 9 mm dia. pyrex tubing, while the center piece is a 12.7 mm dia. x 51 mm long piece of aluminum. The three pieces are held together with 2 sections of Tygon tubing. The center section has a 3.2 mm dia. hole drilled concentrically along its length and the entrance and exit of the piece are cone-shaped. The piece was designed to dampen variations in the magnesium/argon flow. As the density of the magnesium vapor increased and the arc lengthened the flow began to fluctuate, with the fluctuations becoming progressively more severe. Evidence of this unsteady flow is given in Chap. 6 where the magnesium/water vapor reaction is discussed in detail. The center piece was successful in dampening, but did not eliminate the fluctuations.

Although the particles were initially magnesium vapor droplets, thermocouple temperature measurements at the mouth of the transport tube showed that the flow never exceeded 100 °C, indicating that the magnesium had returned to the solid state by the time it left the transport tube. Electron microscopy showed the particles ranged in size from 0.1 to 5 microns, Fig. 3. Table I on the next page gives some relevant properties of magnesium.

Property	Value
Melting Point, K	921.8
Boiling Point, K	1362.8
Latent Heat of Fusion, kJ/mol	8.48
Latent Heat of Vaporization, kJ/mol	128
Density (solid), kg/m^3	1,741
Density(liquid),kg/m^3	1,580
Molecular Weight	24.3

Table I. Properties of Magnesium

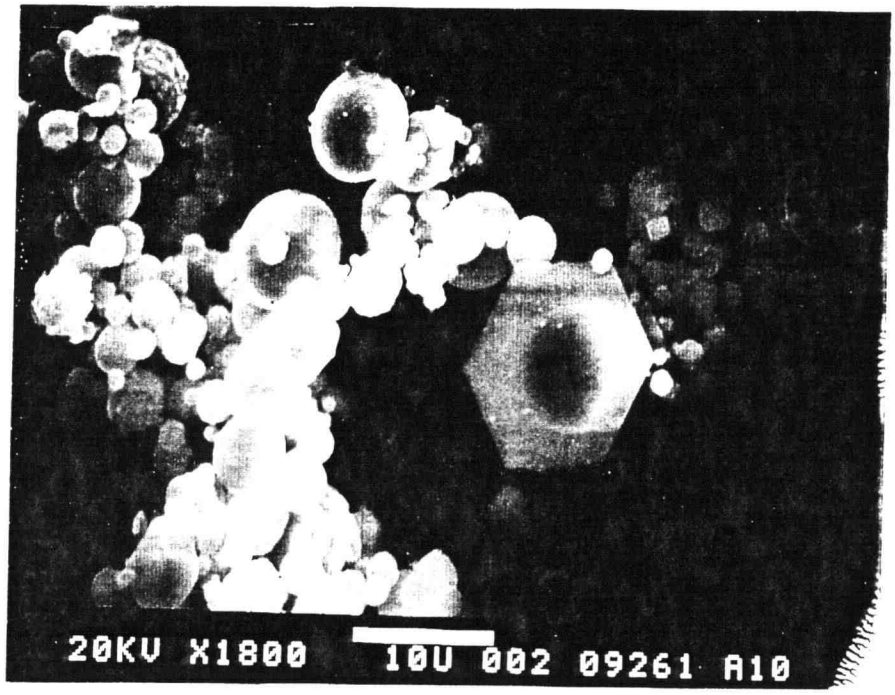

Figure 3. Magnesium Particle Size Photograph

3. BURNER CHARACTERIZATION

The burner designed and used for this study was characterized to determine the flame structure as well as the post flame conditions. This was accomplished by measuring the gas temperature profile over a representative set of tubes for various flow rates of hydrogen and air. A method was developed for measuring the temperature profiles using thermocouples. A numerical model was used to account for the heat losses from the thermocouple bead. This yielded the true gas temperatures from the measured values. The information obtained from the characterization gave the range of oxidizer temperatures available for the synthesis process.

3.1 Experimental Procedure

The burner was housed in a plexiglass chimney 36 x 24 x 53 cm tall. Openings into the enclosure were kept to a minimum to reduce flame movements caused by currents. The bottom of the enclosure was covered with a removable piece of plexiglass while the top of the enclosure, which sat just inside an exhaust fan, was covered with a fine mesh screen. This greatly reduced air movement within the enclosure. Probe access was through a 13 x 13 cm hole in one side of the enclosure. Flexible rubber was placed over the hole and around the probe to restrict airflow.

Temperature measurements were made with a type S (Pt.-Pt.,10% Rh.) thermocouple having wire and bead diameters of 0.13 mm and 0.300 mm, respectively. The thermocouple was mounted in a double-holed ceramic tube, 1 mm in diameter, with 1

cm of wire exposed beyond the end of the tubing. The holes in the ceramic were large enough that the contact between lead wires and tubing was minimal. Measurements with varying lengths of lead wire exposed showed that a length of 1 cm ensured that the presence of the tubing did not interfere with the temperature measurement. A three-direction (x,y,z) translation stage equipped with dial micrometers measuring to the nearest 25 μm was used for positioning of the thermocouple. The temperature was measured for hydrogen/air combustion above the surface of the burner at nominal heights of 0.5, 2, and 4 mm for stoichiometric ratios of 0.5, 1 and 2. Note that stoichiometry in this work refers to the overall flow rate ratios of the fuel and oxidizer, even though the flame sheet for an individual diffusion flame is established at a local equivalence ratio of one.

All experiments were run with the same air flow rate of 1.58×10^{-4} m^3/s and with no flow up the center brass tube. The hydrogen flow rate was adjusted to give the three stoichiometries and varied from 2.17×10^{-5} m^3/s to 8.83×10^{-5} m^3/s. The air and hydrogen flow rates were measured with Matheson rotameter model numbers 604 and 603, respectively. The approximate flow rate needed for ideal stoichiometry was found by determining when the temperature in the post flame gases peaked as the hydrogen flow rate was increased. Starting with a low flow rate of hydrogen, the thermocouple was placed at the location of maximum temperature, which was about 3 mm above the tubes. As the flow rate was increased the thermocouple was raised to stay with the maximum temperature. The conditions were taken to be approximately stoichiometric when the maximum temperature peaked. Once the stoichiometric flow rate was known the other

two stoichiometries could be determined from the ratio of their hydrogen flow rates to that of the stoichiometric flow rate.

In order to determine the thermal conditions above the burner surface, temperature measurements were made for a group of three representative tubes, as shown by the top view of the burner in Fig. 1. For all measurements the lead wires lay in a vertical plane with approximately 0.5 mm in distance between them. Fig. 4 shows the lead wire configuration for the temperature measurements over the tubes. The lead wires were bent in an L shape with the bead at the end of the short section of the L. The lead wire in this short section was equal in length to half the distance between the centers of two tubes (1.65 mm). This placed the junction of the wires at the desired measurement location at the vertical centerline of the three tube set under study. Vertical and horizontal, in this instance and throughout the following description, refer to the orientations of lines on Fig. 4. The longer leg of the L lays between the tubes. For each profile, fifteen equally spaced measurements were taken along the vertical centerline of the tube set.

Raw temperature data from the measurements revealed a profile of shallow maximums and minimums. It was obvious that a correct thermocouple model must include the environment temperature along the entire length of the exposed thermocouple wire. To accomplish this, the temperature profile of the environment between the tubes was determined with another thermocouple probe similar to the first one but with straight lead wires. With this second probe, temperature measurements were taken at several locations between the tubes. The measurements were made in two different directions.

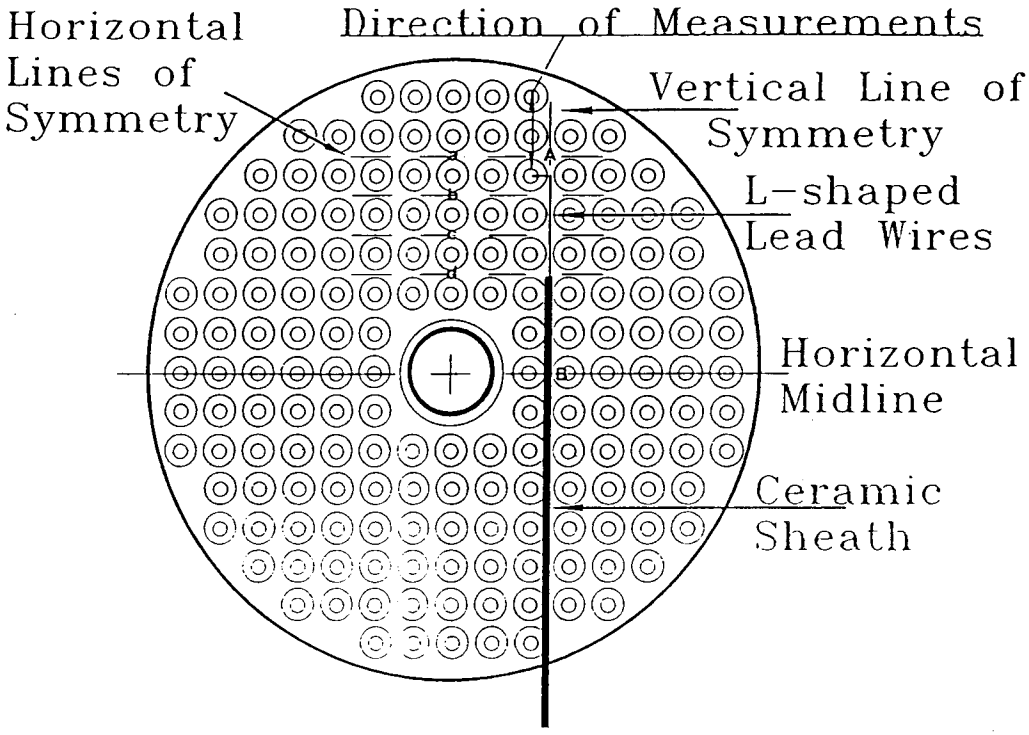

Figure 4. Geometric tube arrangement with horizontal and vertical lines of probing. Thermocouple shown in the L-shaped configuration for measuring the temperature profile over the tubes.

The first involved a line of measurements along the vertical line of symmetry as previously mentioned which gave the temperatures between the tubes. The second was performed along the other direction (orthogonal to the first direction) which yielded a second measurement for some locations. As shown below, the second measurement gave a means for bracketing the temperature environment used in the model.

With the straight thermocouple probe, twelve equally spaced measurements were made along the vertical line of symmetry starting at point A in Fig. 4 and concluding at the horizontal midline of the burner, point B. The measurements made in the orthogonal

direction were made along the four horizontal lines of symmetry in Fig. 4, labeled a, b, c, and d. Six equally spaced measurements were made along the horizontal lines of symmetry starting at the line A-B and ending at the locations of a, b, c, and d in the figure. The pattern for the measurements was the same as the pattern used along the vertical line of symmetry. Note that the points at the right-hand end of the horizontal lines of symmetry were measured twice, once from each direction. Also, the points at the intersection of the vertical centerline of the three tubes and the horizontal lines of symmetry were measured twice, once with the lead wires straight and later with the thermocouple probe having the bent, or L-shaped configuration.

It is well known that platinum thermocouples sheathed in ceramic may lose their calibration when used in reducing environments (Benedict, 1981). As was pointed out above, the contact between the lead wires and ceramic sheath was minimal. However, since water and hydrogen were present in the hot gases the accuracy of the thermocouple was checked periodically throughout the experiment by measuring the temperature of boiling water with the type S thermocouple and comparing with a type K thermocouple. The thermocouples always agreed within 3 °C, and since the accuracy of the type S is $\pm$ 1.5 °C and the accuracy of the type K is $\pm$ 2.2 °C, this was deemed acceptable.

3.2 Thermocouple Model

The analytical model for the thermocouple has two parts, one for the wire and one for the bead. The wire is modeled as a very thin cylinder with a temperature gradient along its length only, while the bead is modeled as a sphere at constant temperature. It

was assumed that no temperature gradients exist within either the bead or across the diameter of the lead wires. Furthermore, the model is for steady state conditions only. To obtain the governing equation, an energy balance was performed for both parts. Note that the objective of the analysis is to determine T_∞, i.e. the temperature of the gas surrounding the thermocouple.

The bead was modeled as a sphere with convection and radiation acting at its surface and conduction at the point of contact between the bead and the thermocouple wires. This gives an algebraic equation

$$4\pi r^2_{bead} h(T_\infty - T_{bead}) = 4\pi r^2_{bead} \sigma \epsilon (T^4_{bead} - T^4_{sur}) - 2\pi r^2_{wire} k \frac{dT_{wire}}{dx}\Big|_{x=0} \qquad (1)$$

where T_∞ is the temperature of the hot gas, T_{sur} is the temperature of the ambient surroundings (for radiation exchange), T_{bead} is the temperature of the bead, and T_{wire} is the temperature of the lead wire. Also in this expression r_{bead} is the radius of the bead, r_{wire} is the radius of the lead wire, σ is the Stefan-Boltzman constant, ϵ is the emissivity of the bead, h is the convective heat transfer coefficient between the bead and surrounding hot gas, and k is the thermal conductivity of the lead wire.

For the wire a differential section was considered with conduction at either end and radiation and convection acting at the surface. The result is the familiar second order differential equation for one dimensional heat transfer in a cylindrical fin

$$\pi r^2_{wire} k \frac{d^2 T_{wire}}{dx^2} = 2\pi r_{wire} h(T_{wire} - T_\infty) + 2\pi r_{wire} \sigma \epsilon (T^4_{wire} - T^4_{sur}) \qquad (2)$$

where ϵ is the emissivity of the wire, which is the same as that of the bead, and h is the

convective heat transfer coefficient between the wire and the surrounding hot gases.

The heat transfer coefficient was determined from the Nusselt number ($Nu = hL_c/k$), where L_c is a characteristic length and k is the thermal conductivity of the gas evaluated at the film temperature. The characteristic lengths for the bead and wire are their respective diameters. Based on the diameter of the quartz tube and reactant properties evaluated at standard conditions, the Reynolds number is less than ten for all flow rates used in this work. At these very low Reynolds numbers the Nusselt number for the sphere is approximately two (Welty et al., 1969). For the wire both forced and natural convection contribute to the heat transfer. Karlekar and Desmond, 1982, give correlations for the Nusselt number for either mode of convection and Nakai and Okazaki, 1975, indicate that the combined Nusselt number is approximately one.

The numerical model divided the thermocouple into a series of nodes with the first node at the junction between the bead and the wires. Boundary conditions were applied to the first and last nodes. Equation (1) was used to describe the first node, and an imposed temperature gradient of zero was used to determine the final node's temperature. The latter of these boundary conditions was selected after determining that only gradients of unrealistic steepness had any effect on the predicted value of T_∞. All nodes between the first and last were modeled using Eq. (2). Equations (1) and (2) were solved to give expressions for the first and following node temperatures.

The model for Eq. (1) was found by using a second order forward difference scheme,

$$\frac{dT_{wire}}{dx}\Big|_{x=0}=\frac{-3T_0+4T_1-T_2}{2\Delta x} \tag{3}$$

Substitution of Eq. (3) into (1) and letting $T_{bead}=T_0$ gives an equation that yields T_0. The solution is simplified by letting $T^4_{bead}=T_0T^3_{0old}$, where T_{0old} is the value of T_0 found by the previous iteration. The result is,

$$T_0=\frac{A_{bead}\Delta x(hT_\infty+\epsilon\sigma T^4_{sur})+A_{wire}k(4T_1-T_2)}{A_{bead}\Delta x\epsilon\sigma T^3_{0old}+3A_{wire}k+hA_{bead}\Delta x} \tag{4}$$

where A_{bead} is the surface area of the bead and A_{wire} is the cross-sectional area of the thermocouple wire. The form of the above expression gives a solution for T_0, yet T_∞ is the desired quantity. The reason this has been done will become clear shortly.

Equation (2) models any node n, such that $T_{wire}=T_n$. Second order central difference was used for the second derivative

$$\frac{d^2T_{wire}}{dx^2}=\frac{T_{n+1}-2T_n+T_{n-1}}{\Delta x^2} \tag{5}$$

T_n can be solved for once Eq. (5) is substituted into Eq. (2). With $T^4_{wire}=T_nT^3_{n\text{-}old}$ this yields

$$T_n=\frac{\left(\frac{T_{i-1}+T_{i+1}}{\Delta x^2}\right)+\left(\frac{4h}{kd_{wire}}\right)T_{\infty,n}+\left(\frac{4\epsilon\sigma}{kd_{wire}}\right)T^4_{sur}}{\frac{2}{\Delta x^2}+\left(\frac{4h}{kd_{wire}}\right)+\left(\frac{4\epsilon\sigma}{kd_{wire}}\right)T^3_{nold}} \tag{6}$$

The boundary condition at the end of the wire simply sets the temperature of the last node equal to the temperature of the previous node,

$$T_N = T_{N-1} \tag{7}$$

Equations (4), (6) and (7) were used to model the thermocouple. The thermal conductivity of the wire and gas, as well as the emissivity of the wire were allowed to vary with temperature. Weast, 1970; Karlekar and Desmond, 1982; and OMEGA ENGINEERING, INC., 1992; provided the needed data to determine a third order fit for these properties. The variation in these properties for the temperature range of the experiment was 74-82 and 0.07-0.10 W/m-K for the thermal conductivities of the wire and air, respectively, and 0.13-0.17 for the emissivity of the bead and wire. The model was run with a node spacing of 0.005 cm for the measurements between the tubes and 0.004 cm for the measurements over the tubes. An approximate error criterion of 1.0×10^{-6} was used for stopping the iterations. Both the node spacing and error criterion were selected to give acceptable predicted temperatures that did not change significantly upon further reductions in these two quantities.

Although the model predicts the temperature of the thermocouple, the goal is to determine the temperature of the hot gas around the thermocouple. In order to use the model, a trial T_∞ must be assumed for the hot gas surrounding the exposed bead and a temperature profile must be assumed for the length of the lead wires. After iterating to a solution for T_0 and the T_n's, the correctly chosen T_∞ gives a predicted bead temperature that corresponds to the measured value.

The first step in determining the flame temperature over the tubes was to determine the profile between the tubes. Unfortunately, more than one profile gave the measured temperatures between the tubes. This is the reason the temperature at the same

location was measured from two different directions. This works because the measured values for a particular location will be different, but regardless of the measurement direction, T_∞ at that point must be the same. Therefore, the profiles used in the model for each direction should begin with the same temperature. Since the rest of the profile for each direction is unique, the correct profiles were those that gave the measured temperature while beginning with the same temperature.

The temperature profiles between the tubes were determined by thermocouple probing along a line midway between two banks of tubes, as described earlier. For the stoichiometries of 0.5 and 1.0, the maximum temperature point was immediately between a pair of tubes on either side of the thermocouple, and the minimum temperature point was at the center of a group of four tubes (along the line of probing). With the numerical model and the assumption of a linear temperature profile connecting the minimum and maximum temperature points, the thermocouple data was analyzed to yield T_∞. For the rich stoichiometry case, the location of maximum and minimum temperature was reversed in the analysis. The switch in the location was due to the distribution of air flow rates around the tubes. If the velocity of air everywhere between the tubes is constant, then the volume of air available for combustion will vary with the cross sectional area of the flow. The point at the center of four tubes represents a maximum flow area. For the lean and stoichiometric cases, air in this region is in excess, which produces a cooling effect. For the rich conditions, however, more hydrogen is available for combustion. This allows more of the air in the high flow rate regions to react giving higher temperatures in this region. Although these assumptions are rather simplistic, as

will be discussed in the later sections, they lead to acceptable uncertainties in the resulting corrected temperature profiles.

Once the profile between the tubes was known, the profile over the tubes was generated. These measurements were taken with a 90° bend in the lead wires, thus most of the thermocouple lay in the known profile between the tubes. Since the gradient over the tubes was most likely not linear, the assumed profile for the environment around the portion of the thermocouple over the tube was broken up into small sections over which linearity was assumed. The sections were determined by the intersection of seven concentric rings with the location of the thermocouple, as shown in Fig. 5. Concentric rings were chosen so that they would correspond to isotherms, but this turned out to be only a rough approximation. By starting with the reading farthest from the center of the tube and using the nearest known temperatures to aid in determining the assumed temperatures for the intersection points, the profile can be generated by starting on the outside and traveling in toward the center of the tube.

3.3 Profiles

The temperature profiles resulting from the analysis of the thermocouple data are shown in Figs. 6-8. They are influenced somewhat by an uneven distribution of air flow within the burner. Section 3.6 discusses the causes for this distribution problem, but it essentially results from an excess of air around the perimeter of the burner and near the center brass tube. Fig. 6 gives the profiles for the lean stoichiometry of $\phi = 0.5$ In general, the profiles show less fluctuation in temperature as the distance from the

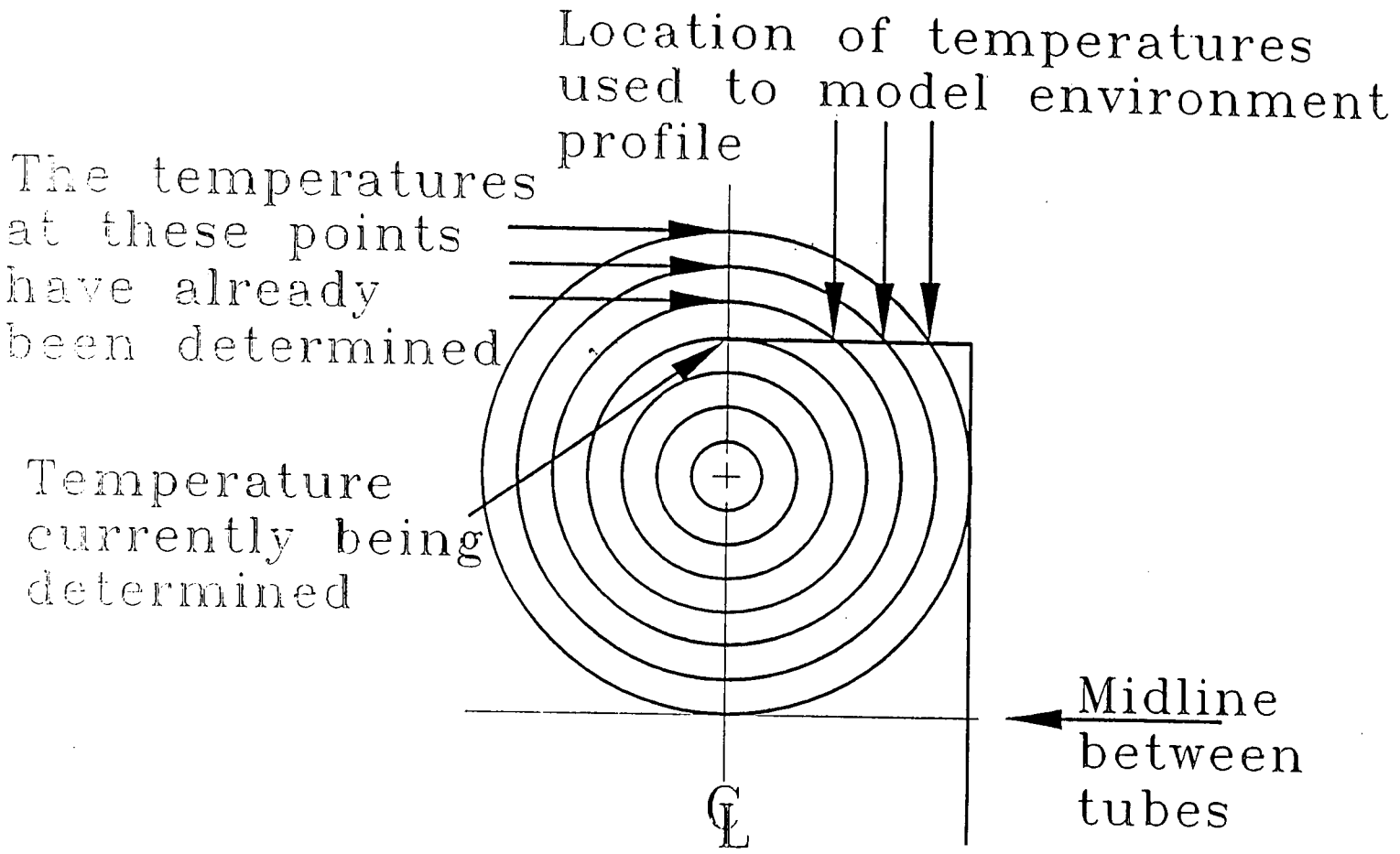

Figure 5. Concentric rings used to generate environment temperature profile for use in model.

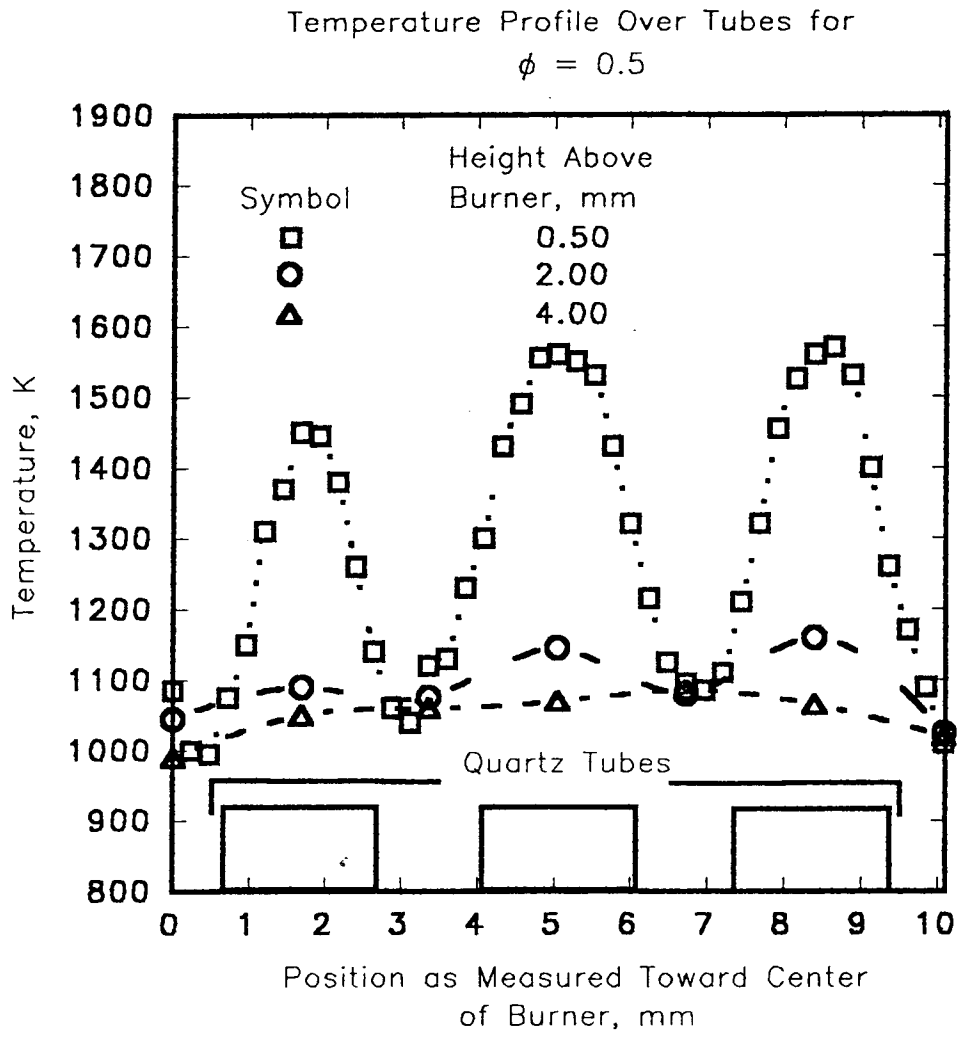

Figure 6. Temperature profiles for ϕ = 0.5

burner increases. This indicates that the burning of the hydrogen takes place very near the outlet of the tubes giving a very short flame. The flatter profiles farther away from the tubes show that the energy generated by combustion quickly distributes itself over the area above the burner as the combustion products travel away from the flame front.

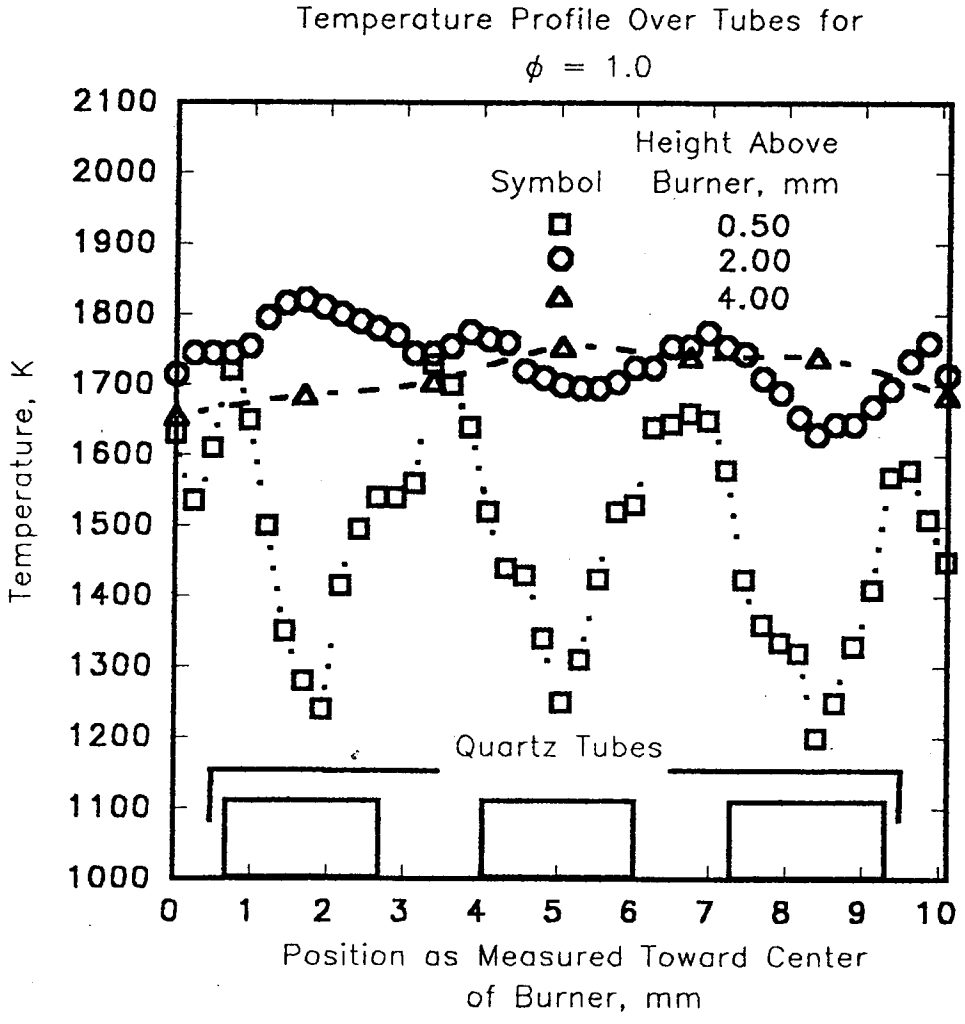

Figure 7. Temperature profiles for ϕ = 1.0

The profiles for a stoichiometry of ϕ=1.0 are given in Fig. 7. The curves have the same trends with height as the lean stoichiometry case and as before the sharpest gradients occur at 0.5 mm. In this case, however, the peak temperatures at 0.5 mm occur between the tubes and the minimum temperatures are at the center of the tubes.

At a height of 2 mm most of the maximums are still between the tubes, indicating that the height of the flames is in excess of 2 mm. At a height of 4 mm the temperature distribution has flattened out.

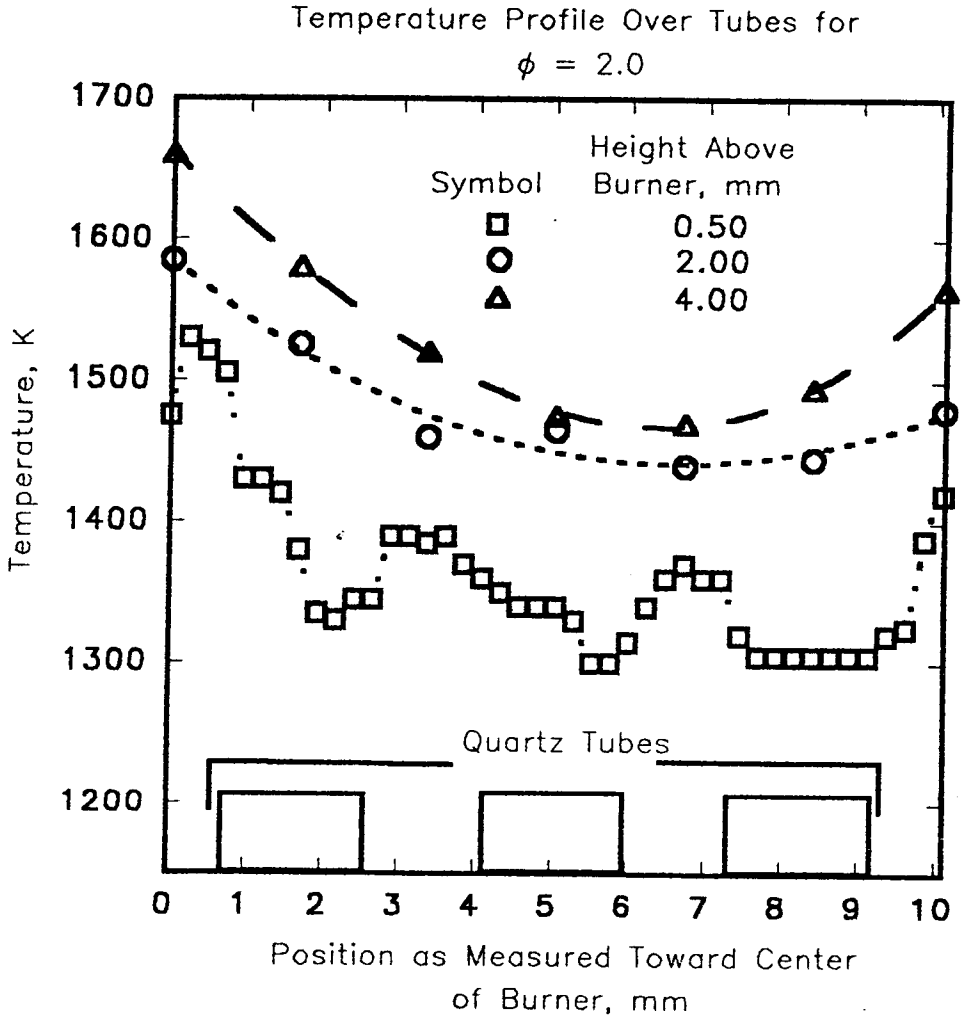

Figure 8. Temperature profiles for ϕ = 2.0

Fig. 8 shows a stoichiometry of $\phi=2$. The curves clearly demonstrate the effect caused by excess air. Immediately above the tubes (0.5 mm data), there are pronounced maximums between the tubes and minimums over the tubes, but these are no longer observed at 2 mm, indicating that the height of the flames decreased as the flow rate of hydrogen was increased. Because of the unexpected difficulty in creating a well characterized post combustion region for the $\phi=2$ case, the temperature profiles are presented here but will not be discussed and analyzed.

3.4 Shapes and Heights of the Flames

The Reynolds numbers of the flames indicate that they are in the laminar regime. The approximate relative velocities of fuel to air for the lean, stoichiometric, and rich flames are, respectively, 1:1, 2:1, and 4:1. Flame stoichiometry as well as the reactant velocities will determine the shape and height of the flames. The temperature profiles in Figs. 6-8 reflect information about the heights and shapes of these three different laminar diffusion flames.

Burke and Schumann, 1928; first demonstrated, and explained theoretically, that overventilation gives a closed flame while underventilation produces an open flame. These observations pertain to concentric flow of fuel and oxidizer with fuel flowing in the center. Theoretically, the flame at an ideal mixture ratio would be open and infinitely tall. Practically speaking, however, it must have some finite height. Burke and Schumann, 1928; also showed that increasing the fuel flow rate increases the height of an overventilated flame and decreases the height of an underventilated flame.

Expressions were derived for the height and shape of a single flame using Bessel functions. Later, Roper, 1977a and Roper, 1977b; produced a simplified solution showing that the flame height for a circular port burner is independent of secondary air velocity. However, Roper's work only applies to overventilated flames. In a subsequent paper Roper, 1979; studied a multiple burner system and found that flame height increased if the centers of the burners were moved within a critical separation distance that depended on the radius and stoichiometry of the flame. But again, his work was done only for overventilated flames.

The diffusion flames for $\phi = 0.5$ are overventilated with approximately equal velocities of hydrogen and air. The theoretically predicted shape should be closed similar to a candle flame. The reduced experimental profiles from this work support this point. The 0.5 mm profile in Fig. 6 shows very steep gradients with cooler temperatures between the tubes and peak temperatures over the center of the tubes. An open flame would have just the opposite profile. The maximum temperatures over the centers of the tubes suggests that the measurements were taken near or above the tips of the diffusion flames and so their height is approximately 0.5 mm or less.

For the stoichiometric case the temperature profile measured at 0.5 mm shows maximums between the tubes and minimums at the center of the tubes. That is, the maximums between the tubes correspond to the edges of the flames and the minimums at the center correspond to the region within the flame where the hydrogen is flowing towards the flame front but is as yet unburned. At 2 mm minimums still occur at the center of the tubes, but the gradients are not nearly as steep. Also, the maximum

temperatures are about the same as for the 0.5 mm profile. The measurements seem to have been taken slightly beneath the maximum flame height. For the tube nearest the outer edge the maximum is near the center of the tube and the minimums at the edges are about the same as the maximums of the 0.5 mm profile. This suggests that the flame closes and that its height is about 2 mm. It cannot, however, be inferred that the other two flames close. Due to the uneven air flow distribution the outer tube appears more ventilated, and therefore the flame would likely close.

Although the profiles in Figs. 6-8 are not intended to be used for precise determination of the heights and shapes of the flames, they should reflect the change in height and shape with fuel flow rate. Each individual flame could be seen as a circular burner in a square tube, similar to Burke and Schumann's circular burner in a circular tube. However, the "walls" of the square tube are moving gases and for both the stoichiometric and rich cases the flames compete with one another for the oxidizer. As Roper, 1979; has pointed out, this competition can lengthen the flame. Thus, although the geometry and flow conditions differ from the classic Burke-Schumann arrangement, it seems that the flames should follow similar trends. This has been found to be the case. The lean flames are shortest. The stoichiometric flames are much taller and wider. As richer conditions are approached, they again shorten while maintaining a wide profile.

3.5 Uncertainty Analysis

The trends in the profiles as well as the magnitude of the temperatures appear reasonable. The maximum flame temperatures are well below the adiabatic flame temperatures of 1655, 2387, and 2069 K, respectively, for the lean, stoichiometric, and rich flame systems (based on overall stoichiometries). The trends in temperature with changes in mixture ratio are as expected, with the highest temperatures found under stoichiometric conditions. The maximum temperature for the rich case should be greater than for the lean flames, which is not the case. However, it is not certain that the maximum temperature of the rich flame system was measured.

The difference between maximum and adiabatic flame temperatures also appears reasonable, given the factors contributing to the differences. The flames lose energy by radiation to the surroundings and by conduction to both the burner tubes and downstream into the post combustion gases. Measurements of the oxidizer temperature just below the surface of the tube bundle indicated temperatures around 800 K. Also, the measurement technique itself will lower the measured peak temperature due to the averaging effect of having a thermocouple bead of finite size and having two thermocouple leads that are at slightly different heights than the bead. The numerical model used to determine T_∞ neglects these effects.

There are also uncertainties in the measurements themselves which propagate through the analysis process to affect the corrected environment temperature. Repetitive measurements in the region where the most severe gradients occur indicate the measured values will vary a maximum of ± 10 K. This is caused by small changes in flow rate of

fuel and/or oxidizer and spurious air currents around the burner. Error associated with the thermocouple measurement is approximately $\pm$ 0.25% of the reading, which would be a maximum of 3.5 K Thus the uncertainty of the measurement overshadows any error in the latter one.

As indicated earlier, some of the temperatures between the tubes were found from two profiles measured in different directions. The temperatures determined from these two profiles varied by a maximum of 60 K, which gives an upper bounds to the uncertainty in the assumed profile between the tubes. It takes a change of approximately 5 K in the assumed temperature to effect a 1 K change in the predicted temperature so that the 10 K uncertainty in the measurement will result in a 50 K change in the assumed temperature. For the worst case the uncertainty in the predicted values between the tubes would be $\pm$ 80 K

The analysis procedure yielding T_∞ over each tube is influenced by both the profile between the tubes and the temperature measurements over the tubes themselves. This is further emphasized in the following. For measurement over the tubes, most of the thermocouple is exposed to the environment between the tubes. The temperature for this region has been determined by independent thermocouple measurements. Furthermore, during a measurement, the temperature profile being generated over the tube is influenced by the values of the nearest temperatures already determined. For example, the first over-the-tube temperature is based, in part, on the temperature one position away at the midpoint between the tubes and the thermocouple reading itself. The next temperature two locations removed from the midpoint, is based on the measured

temperature, the temperature one position away from the midpoint, and the midpoint temperature (along the temperature profile between the tubes). The process proceeds in this way to build up the temperature profile over the tubes. The largest effect on the model is the changing temperature gradient in the thermocouple lead wires near the bead. Based on numerical experimentation with the thermocouple model, the uncertainty in the temperatures over the tubes resulting from variations in the temperature profiles for the lead wires is $\pm$ 100 K.

Another source of error results from the uncertainty of the property values used in the model. Enough data exists for the thermal conductivity of air and platinum to give good confidence in the curve fits used for these properties. However, reliable values for the emissivity of platinum under the conditions of this experiment are not available. Considering the range of values the emissivity can assume under flame conditions, this property could be off by as much as 20 % in the numerical model. Varying the emissivity by this amount for the thermocouple bead caused a change of 10 K in the temperatures of the hottest environments. However, with the uncertainty in the emissivity folded into the most sensitive part of the analysis, namely the temperature gradient in the lead wires near the bead, the uncertainty is $\pm$ 50 K. A worst case scenario would be an addition of this value with the one discussed in the previous paragraph. This would give a maximum uncertainty in the profiles of Figs. 6-8 of $\pm$ 150 K The uncertainty is greatest for the highest temperature profiles and has a minimum of 100 K for the lowest temperature profiles. The uncertainty, then, is approximately $\pm$10%.

Although the profiles may be off by as much as 150 K the shapes of the profiles are reliable. Numerical experimentation showed that the profile temperatures nearest the bead had predominant control over the temperature of the bead produced by the model. This can be taken to reflect the actual situation, where the environment near the bead is controlling, for the most part, the temperature of the bead. It is reasonable to assume, then, that the trends of the measured profile are the actual trends in the temperature profile. Since the profiles produced by the model have the same trends as the measured profiles the profiles of Figs. 6-8 give the true shape of the temperature profiles.

3.6 Improvements in the Burner

The general design of the burner is sound, but improvements can be made in oxidant distribution around the quartz tubes. The distribution is impaired by holes around the center hole and edge of the second screen. Since the space between the tubes and brass screen is very small, there is a disproportionate amount of oxidant flow in the center and around the periphery of the burner.

The brass perforated sheets were cut from a large sheet of screen, leaving several partial holes along the outside edge of the circular disk and along the inside circular opening. This causes the distribution to become skewed by a disproportionate flow of air through the small gaps at the inner and outer edges of the burner. Hot wire anemometer measurements above the surface of the burner revealed the excessive flow regions. Another improvement would result by distributing the oxidizer flow through four equally spaced fittings placed around the periphery of the burner. This would

further enhance the uniformity of the oxidizer flow thus providing an even temperature and composition region downstream from the burner surface.

CHAPTER 4. PARTICLE STREAM DIFFUSION FLAME MODEL

Particle burning has received varying degrees of attention over the past 30 years. In the 60's and early 70's, solid propellant rocket research drove the need to understand how individual particles burn (Fassel, 1960; Gordon, 1960; Markstein, 1963; Brzustowski and Glassman, 1964) and over the past two decades the desire to understand pulverized coal combustion has fostered research on particle cloud burning (Smoot, 1977). Whether individual or groups of particles are considered, most studies have focused on configurations where the particles and oxidizer are well-mixed, each particle being completely surrounded by oxidizer. This type of burning has been modeled for both individual and streams of particles (Brzustowski and Glassman, 1964; Markstein, 1964; Law, 1973; Smoot,1977; Kashireninov, 1990).

This chapter introduces a flame profile model for the parallel flow configuration of particle stream combustion. The geometry is that associated with typical gaseous diffusion flames. The fuel particles flow in an inert carrier in parallel to a hot oxidizing environment as shown in Fig. 9. The result is a diffusion limited flame between the particle stream and oxidizer. The model is based on species conservation for the oxidizer and a stoichiometric balance of fuel and oxidizer at the flame front.

4.1 Flame Model

A two-dimensional model was developed for cartesian geometry and a similar approach was considered for the cylindrical coordinate system, Figs. 10 (a) and (b). The

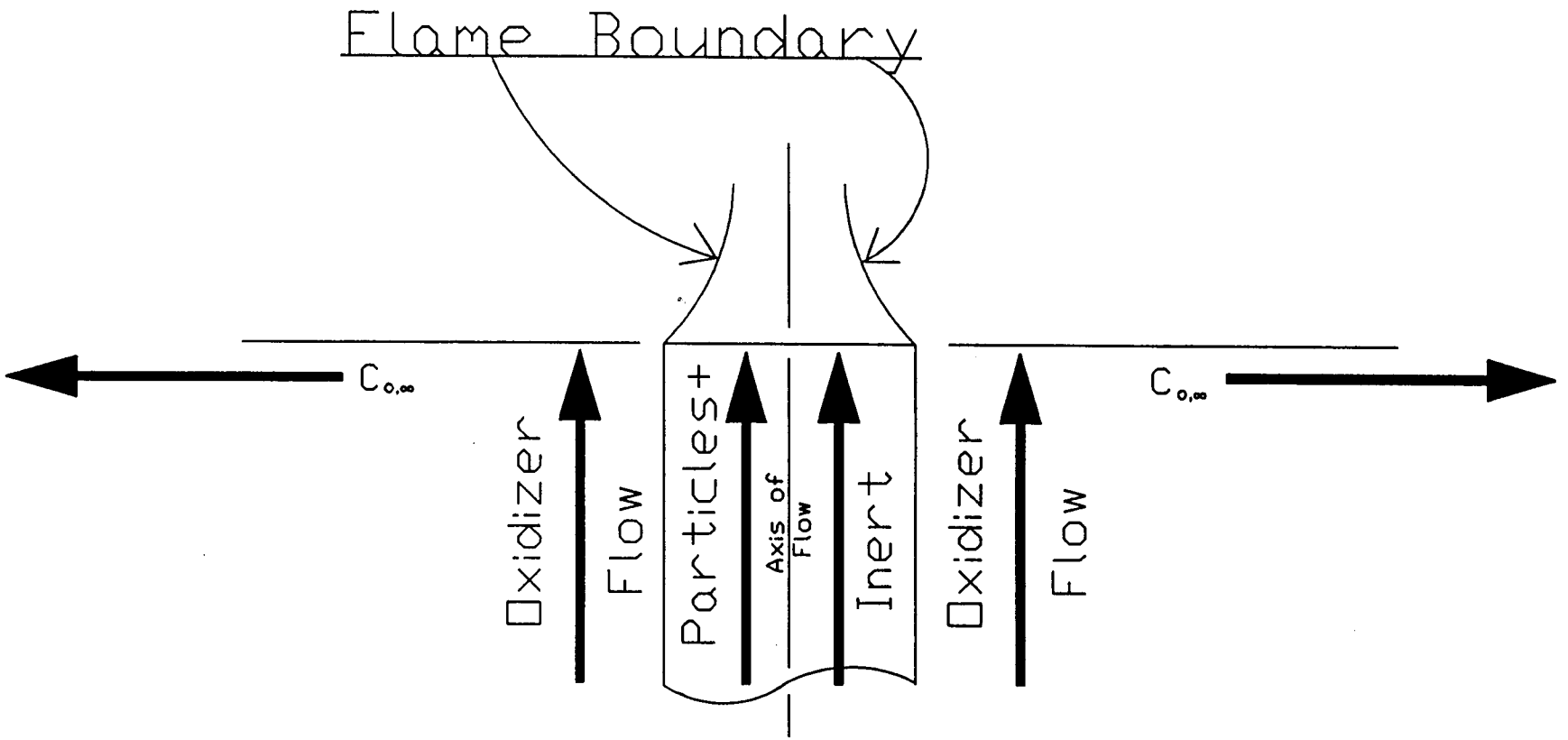

Figure 9. Model Geometry

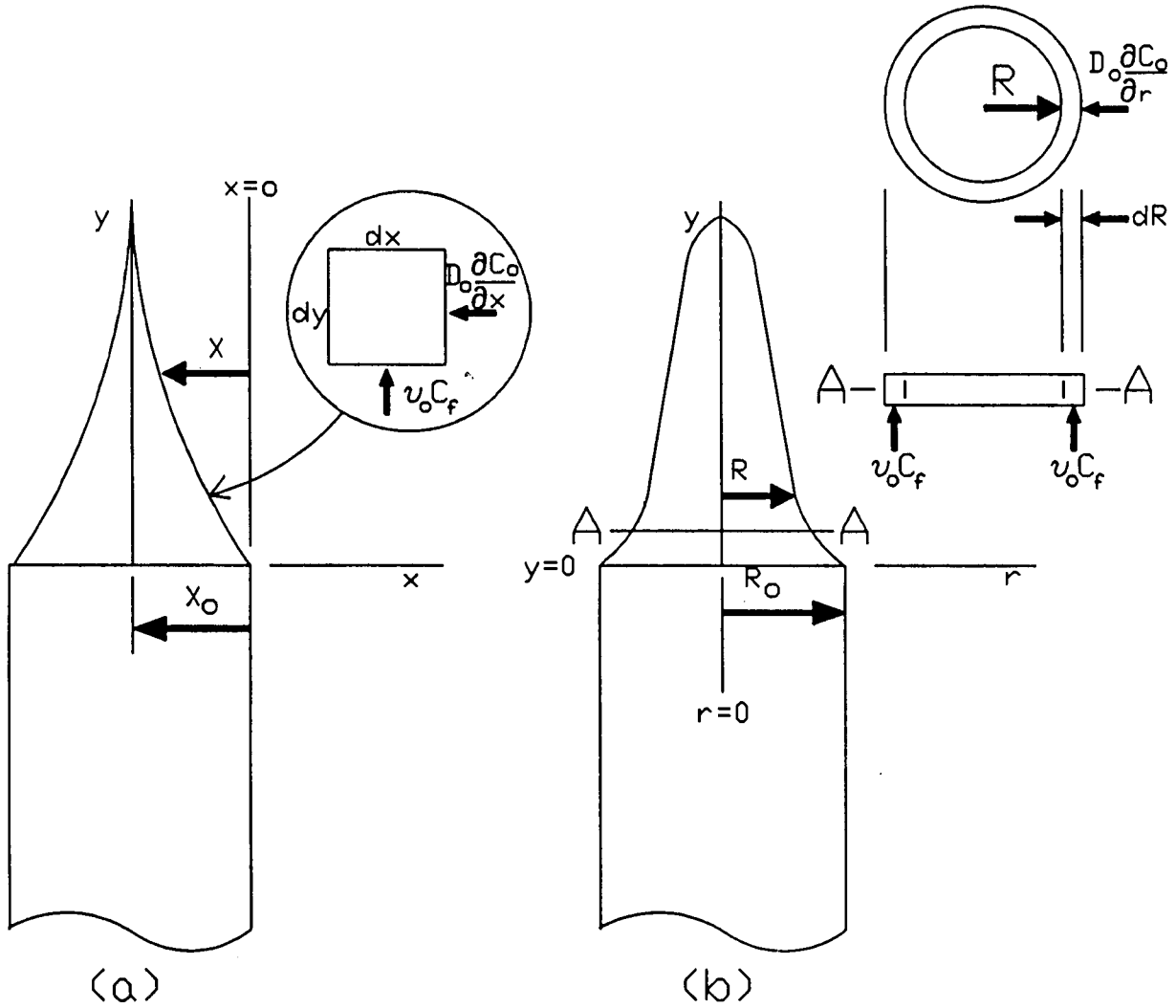

Figure 10. Coordinate Systems: (a) Cartesian and (b) Cylindrical

cartesian geometry has infinite depth into the paper. The oxidizer for both coordinate systems extends to infinity away from the center particle flow. In the freestream, the oxidizer concentration and flow are uniform, Fig. 9. The initial concentration of the oxidizer is $C_{o,\infty}$. The beginning of the freestream is the location where the concentration of the oxidizer is equal to the initial concentration. This definition of freestream conditions lends itself to the use of a dimensionless concentration variable θ. It is defined as the ratio of the oxidizer concentration at any point in the flow, C_o, to that of the freestream concentration $C_{o,\infty}$. The reaction kinetics are assumed to be infinitely fast compared to the rate of oxidizer diffusion such that the oxidizer is completely consumed as fast as it reaches the reaction front. This means the variation in C_o is from zero at the reaction boundary to $C_{o,\infty}$ at the freestream. The corresponding variation in θ is from zero to one.

Other assumptions include:

a) constant and equal velocities for inert carrier, particles and oxidizer,

b) constant diffusion coefficient,

c) no thermal effects, and

d) steady-state.

A key difference between the two coordinate systems is the location of the origin. Note that in the cartesian coordinate system, the origin is located at the beginning of the interface between particle stream and oxidizer, whereas the origin for the cylindrical coordinate system is at the middle of the particle tube. The placing of the origin at the beginning of the interface facilitates the analysis for the cartesian system but the origin

for the cylindrical coordinate system is placed at the center of the particle transport tube to correspond to a radius of zero.

4.2 Cartesian Coordinate System

The basis for the model is a stoichiometric balance of fuel and oxidizer at the interface of particle stream and oxidizer flow, Fig. 9. The oxidizer is assumed to flow into the fuel and completely consume it at a rate equal to the molar mass flow rate of fuel times the stoichiometry. The inset to Fig. 10(a) shows an element of unit depth at the particle/oxidizer interface and the flow of fuel and oxidizer into this element. The molar flow rate for each is the product of the flux that moves into the differential element and the cross-sectional area that the flux passes through as it enters the element. For the oxidizer and particle flows the areas are dy and dx, respectively. The diffusive oxidizer flux is the product of the oxidizer concentration gradient $\partial C_o/\partial x$ and the diffusion coefficient D_o. The flux of fuel into the element is $v_o C_f$,, where v_o is the axial flow velocity and C_f the fuel concentration . The diffusion of the particles is assumed to be negligible. This last assumption gives this model its uniqueness and sets it apart from typical gaseous diffusion flame models which must account for the diffusion of both oxidizer and fuel. A comparison of the rate of diffusion for particles and gas species provides the justification for this assumption.

The diffusion of the particles relative to the oxidizer is assumed to be negligible because of the relative size of the particles. The particles considered in this work can be approximated by spherical objects of the order of microns in diameter. Particles of

this size will diffuse by Brownian motion. McQuarrie, 1976, gives the diffusion coefficient for Brownian motion as

$$D=\frac{kT}{6\pi a\nu} \tag{8}$$

where k is Boltzmann's constant, T is the absolute temperature, a is the particle radius, and ν is the viscosity of the fluid surrounding the particle. The viscosity for an inert gas such as argon at a temperature of 1000 K is of the order of $1x10^{-5}$ kg/m-s. At this temperature a particle one micron in diameter would have a Brownian diffusion coefficient of $1x10^{-6}$ cm^2/s. For a typical gaseous oxidizer species at the same temperature the diffusion coefficient based on the Chapman-Enskog equation or empirical correlations (Cussler, 1984) would be of the order of 1 cm^2/s. In order for the diffusive flux of the particles to be comparable to that of the gaseous species the mass density gradient of the particles would have to be one million times greater than that of the gas. Clearly, the assumption of negligible particle diffusion is well justified.

The fuel and oxidizer combine in stoichiometric ratio at the flame front. So the flow rate of fuel is equal to the product of the stoichiometric ratio of fuel to oxidizer, f_{st}, and the diffusion rate of oxidizer

$$C_f v_o dx = f_{st} D_o \frac{\partial C_o}{\partial x} dy \tag{9}$$

Equation (9) can be expressed in terms of the dimensionless variable θ by dividing through by the freestream concentration of the oxidizer $C_{o,\infty}$

$$f_{supp} v_o dx = f_{st} D_o \frac{\partial \theta}{\partial x} dy \qquad (10)$$

where f_{supp} is the concentration ratio of fuel to oxidizer at inlet (supply) conditions, $C_f/C_{o,\infty}$. This gives a relationship between the width of the flame x and the height y in terms of known or measurable parameters and the dimensionless concentration gradient of the oxidizer. Another equation is needed that relates θ and x so that y can be cast as a function of x alone. The equation comes from considering the conservation of the oxidizer species.

Conservation of a species means that its change in concentration within a given volume is equal to the net movement of species into the volume plus the net production of species within the volume. Consider a differential volume element (dx)(dy)(1) in the oxidizer flow. The oxidizer moves through the element as it flows in parallel to the fuel, but there is also diffusive movement of oxidizer toward the flame front. This latter movement causes the greatest concentration change within the element because it is the only direction in which the concentration gradient is significant. Also, the oxidizer is neither created or destroyed. The conservation of species equation becomes

$$\frac{\partial \theta}{\partial t} = D_o \frac{\partial^2 \theta}{\partial x^2} \qquad (11)$$

Substitution can be made for dt by recognizing that the velocity v_o is dy/dt so that $dt = dy/v_o$. With this replacement the conservation of species in cartesian coordinates is

$$\frac{\partial\theta}{\partial y}=\frac{D_o}{v_o}\frac{\partial^2\theta}{\partial x^2} \tag{12}$$

which gives a second equation in terms of θ, x, and y. This is the governing partial differential equation for oxidizer diffusion.

Three boundary conditions are needed to solve Eq. (12). The freestream condition provides one of the boundaries. Referring to Figs. 1 and 2a, θ goes to one as x becomes very large. The second boundary condition occurs at the edge of the flame where the concentration of oxidizer is zero and therefore θ is zero. The final boundary condition is Eq. (10). Written in terms of X(y), the location of the flame front, these boundary conditions become,

(a) at $x=\infty$ $\theta=1$

(b) at $x=X(y)$ $\theta=0$

(c) at $x=X(y)$

$$f_{supp}v_o\frac{dX}{dy}=-f_{st}D_o\frac{\partial\theta}{\partial x}\Big|_{x=X(y)}$$

Equation (12) was solved using similarity analysis. The approach is Neumann's first solution for finding the increase in the thickness of a slab as its adjacent liquid solidifies (Carslaw and Jaegar, 1959). The similarity variable was derived by performing scale analysis on Eq. (12). As already discussed θ is of the order of one. The parameters D_o and v_o are constants and x and y scale as themselves. The resulting equation is

$$\frac{1}{y}=\frac{D_o}{v_o x^2} \tag{13}$$

Grouping all the terms together and taking the square root gives a dimensionless similarity variable

$$\eta = \frac{x}{2}\sqrt{\frac{v_o}{D_o y}} \tag{14}$$

The 1/2 simplifies the following analysis.

Applying the similarity variable analysis to Eq. (12), the partial differential equation transforms to an ordinary differential equation in η,

$$-2\eta\frac{d\theta}{d\eta} = \frac{d^2\theta}{d\eta^2} \tag{15}$$

The boundary conditions must also transform. Since η is proportional to x as x becomes infinite, so does η. At the boundary of the flame x=X(y) so $\eta=\eta_X=X/2(v_o/D_oy)^{1/2}$ and the $\partial\theta/\partial x$ at x=X becomes an ordinary differential $1/2(v_o/D_oy)^{1/2}d\theta/d\eta$ evaluated at η_X. Making these substitutions in the boundary conditions yields

(a) at $\eta = \infty$ $\theta = 1$

(b) at $\eta = \eta_X = (X/2)(V/D_oy)^{1/2}$ $\theta = 0$

(c) at $\eta=\eta_X$ $$\frac{dX}{dy} = -\frac{f_{st}}{2f_{supp}}\sqrt{\frac{D_o}{v_o y}}\frac{d\theta}{d\eta}\Big|_{\eta_X}$$

Separating Eq. (15) into terms of $d\theta/d\eta$ and η and integrating once gives

$$\frac{d\theta}{d\eta} = A\exp(-\eta^2) \tag{16}$$

where A is a constant of integration. Integrating again gives

$$\theta = A\int_0^{\eta} \exp(-\eta^2)d\eta + B = A\frac{\sqrt{\pi}}{2}\text{erf}\eta + B \tag{17}$$

where B is a second constant of integration. Using boundary condition (a) where η is infinite and θ is unity, Eq. (17) becomes

$$1 = A\frac{\sqrt{\pi}}{2}\text{erf}(\infty) + B \tag{18}$$

Or solving for B

$$B = 1 - A\frac{\sqrt{\pi}}{2}\text{erf}(\infty) \tag{19}$$

Substituting for B in Eq. (17) gives an expression for θ in terms of A and η. Noting that the argument of the error function terms are infinity and η, the result will be in terms of the complimentary error function,

$$\theta = 1 - A\frac{\sqrt{\pi}}{2}\text{erfc}(\eta) \tag{20}$$

Applying boundary condition (b) to Eq. (20) will give a relationship between X and y. This boundary condition says that at $\eta = \eta_x$, $\theta = 0$. Substituting these values into Eq. (20) yields

$$0=1-A\frac{\sqrt{\pi}}{2}\text{erfc}(\eta_X) \tag{21}$$

or substituting for η_x and rearranging

$$1=A\frac{\sqrt{\pi}}{2}\text{erfc}\left(\frac{X}{2}\sqrt{\frac{\upsilon_o}{D_O y}}\right) \tag{22}$$

Equation (22) must be true for all values of X. Since the left hand side of the equation is a constant, the right side must be as well. For this to be true the argument of the error function must be a constant so that X must be proportional to $y^{1/2}$. Let

$$X=2\lambda\sqrt{\frac{D_o y}{\upsilon_o}} \tag{23}$$

where λ is a constant to be determined.

The constant **A** can be found by using Eq. (23) to substitute for X in Eq. (22). This yields

$$A=\frac{2}{\sqrt{\pi}\,\text{erfc}(\lambda)} \tag{24}$$

Then, **A** can be substituted into Eq. (20) to give an expression for the dimensionless concentration profile for the oxidizer $\theta(\eta)$,

$$\theta(\eta)=1-\frac{\text{erfc}(\eta)}{\text{erfc}(\lambda)} \tag{25}$$

Equations (23) and (35) give the flame and oxidizer concentration profiles, respectively, in terms of λ. Boundary condition (c) is used to determine λ as follows.

If Eq. (24) is used to substitute for A in Eq. (16), an expression for $d\theta/d\eta$ results that can be used in boundary condition (c). Noting that the derivative is evaluated at η_x the result is an equation in terms of X and y

$$\frac{dX}{dy} = -\frac{f_{st}}{\sqrt{\pi}\,\mathrm{erfc}(\lambda) f_{supp}} \sqrt{\frac{D_o}{\upsilon_o y}} \exp\left(-\frac{X^2 \upsilon_o}{4 D_o y}\right) \tag{26}$$

Differentiating Eq. (23) gives $dX/dy = \lambda(D_o/\upsilon_o y)^{1/2}$. Using Eq. (23) and its derivative in Eq. (26) yields an expression in terms of lambda

$$\lambda = -\frac{f_{st}}{\sqrt{\pi}\,\mathrm{erfc}(\lambda) f_{supp}} \exp(-\lambda^2) \tag{27}$$

Or grouping all terms with λ

$$\frac{\exp(-\lambda^2)}{\lambda\,\mathrm{erfc}(\lambda)} = -\phi_D \sqrt{\pi} \tag{28}$$

where Φ_D is the ratio of f values, f_{supp}/f_{st}.

The complete set of equations for this flame are Eq. (28), an expression that can be solved for lambda, Eq. (25), the dimensionless concentration profile, and Eq. (23), the flame profile. Note that Eq. (28) has a solution only for negative values of λ. This is in agreement with the definition of X , which is defined as measured in the negative x direction, and Eq. (23), which gives the flame profile. Note that Eq. (23) gives the flame profile with respect to the fuel supply tube rim. The flame profile with respect to the centerline of the supply tube is X_o+X.

For an example of how Eq. (28) is solved for lambda, let Φ_D=0.5. This makes the right hand side of the equation -0.886. By assuming a value for λ the left hand side of Eq. (28) can be evaluated. Note that the value for λ will be negative and that the compliment error function of $-\lambda$ is $1+\text{erf}(\lambda)$. Table II below shows how λ varies with Φ_D.

Φ_D	λ
0.25	-0.75
0.50	-0.54
0.75	-0.43
1.00	-0.36
1.50	-0.27
2.00	-0.22
3.00	-0.16
4.00	-0.13
5.00	-0.10

Table II. Values of λ as a function of Φ_D

4.3 Cylindrical Coordinate System

A similar analysis was attempted for the cylindrical coordinate system, Fig. 10(b), but the resulting solution presented difficulties in the determination of λ. The flame was modeled as axially symmetric, varying only in r and y. In this case the net diffusive flux yields an additional derivative in the conservation of species equation

$$\frac{\partial\theta}{\partial y}=\frac{D_o}{v_o}\left(\frac{\partial^2\theta}{\partial r^2}+\frac{1}{r}\frac{\partial\theta}{\partial r}\right) \tag{29}$$

The 1/r term is a result of the variation with r of the differential volume in the cylindrical system. Note that as in Eq. (12) dt has been replaced by dy/v_o. Scale analysis of this equation yields a similarity variable similar to that found for the cartesian coordinate system

$$\eta'=\frac{r}{2}\sqrt{\frac{v_o}{D_o y}} \tag{30}$$

Substituting for the partial derivatives in Eq. (29) gives as before an ordinary differential equation in terms of η'

$$-\left(2\eta'+\frac{1}{\eta'}\right)\frac{d\theta}{d\eta'}=\frac{d^2\theta}{d\eta'^2} \tag{31}$$

and the boundary conditions become

(a) at $\eta'=\infty$ $\theta=1$

(b) at $\eta'=\eta'_R$ $\theta=0$

(c) at $\eta'=\eta'_R$

$$\frac{dR}{dy}=-\frac{1}{2\phi_D}\sqrt{\frac{D_o}{v_o y}}\frac{d\theta}{d\eta'}\Big|_{\eta'_R}$$

The solution of Eq. (31) proceeds the same as the solution of Eq. (15). Equation (31) can be separated and integrated once to yield,

$$\frac{d\theta}{d\eta'} = \frac{A' \exp(-\eta'^2)}{\eta'} \tag{32}$$

where A′ is a constant of integration. Eq. (32) is identical to Eq. (16) for the cartesian coordinate system except for η' in the denominator of the right hand side.

Separating and integrating again gives

$$\theta = A' \int_0^{\eta'} \frac{\exp(-\eta'^2) d\eta'}{\eta'} + B' \tag{33}$$

where B′ is a second constant of integration.

Applying boundary condition (a) gives,

$$B' = 1 - A' \int_0^{\infty} \frac{\exp(-\eta'^2) d\eta'}{\eta'} \tag{34}$$

Equation (34) can be substituted into Eq. (33) to yield an expression for θ in terms of η' and A′. Application of boundary condition (b) then gives a correlation that can be solved for A′

$$0 = 1 - A' \int_{\eta'_R}^{\infty} \frac{\exp(-\eta'^2) d\eta'}{\eta'} \tag{35}$$

For Eq. (35) to be true η'_R must be a constant, since all other terms in the equation are constants and the upper limit of integration is constant. Let

$$\eta'_R = \frac{R}{2}\sqrt{\frac{v_o}{D_o y}} = \lambda' \tag{36}$$

Substituting λ' for η'_R in Eq. (35) gives A'

$$A' = \frac{1}{\int_{\lambda'}^{\infty} \frac{\exp(-\eta'^2)d\eta'}{\eta'}} \tag{37}$$

and the dimensionless concentration profile becomes

$$\theta(\eta) = 1 - \frac{\int_{\eta'}^{\infty} \frac{\exp(-\eta'^2)d\eta'}{\eta'}}{\int_{\lambda'}^{\infty} \frac{\exp(-\eta'^2)d\eta'}{\eta'}} \tag{38}$$

Once λ' is known Eq. (38) can be solved using numerical integration.

Boundary condition (c) gives an equation for λ'. To use this boundary condition $d\theta/d\eta'$ at η'_R must be determined. From Eqs. (32) and (37)

$$\frac{d\theta}{d\eta'}\Big|_{\eta'_R} = \frac{\frac{\exp(-\eta'^2_R)}{\eta'_R}}{\int_{\lambda'}^{\infty} \frac{\exp(-\eta'^2)d\eta'}{\eta'}} \tag{39}$$

Boundary condition (c) becomes

$$\frac{dR}{dy} = -\frac{1}{2\Phi_D}\sqrt{\frac{D_o}{v_o y}}\,\frac{\dfrac{\exp(-\eta'^2_R)}{\eta'_R}}{\displaystyle\int_{\lambda'}^{\infty}\frac{\exp(-\eta'^2)d\eta'}{\eta'}} \tag{40}$$

From Eq. (35) $dR/dy = (D_o/v_o y)^{1/2}\lambda'$. Substituting this expression for dR/dy and λ' for η'_R in Eq. (40) and rearranging gives

$$2\Phi_D = -\frac{\dfrac{\exp(-\lambda'^2)}{\lambda'^2}}{\displaystyle\int_{\lambda'}^{\infty}\frac{\exp(-\eta'^2)d\eta'}{\eta'}} \tag{41}$$

The difficulty with this analysis arises with Eq. (41). The right hand side of the equation will always be negative regardless of the sign of λ'. The numerator is obviously always a positive quantity and the integral in the denominator is always positive as well. Since the left hand side is a positive constant an inequality exists. The problem seems to originate from trying to determine the decrease in the length of R as measured from the origin when in fact the change in R should be measured as growth from the rim of the supply tube. That, however, is equivalent to shifting the origin of the supply tube rim, which obviously is not correct. Several attempts have been made at reconciling this problem, but a solution has not been derived.

4.4 Model Results for the Cartesian Coordinate System

Figures 11 and 12 show the flame profile for various combinations of $v_o d^2/D_o$ and Φ_D for the cartesian coordinate system. To reiterate, Φ_D is the ratio of the supply concentration ratio to the stoichiometric concentration ratio for fuel and oxidizer. Figure 11 shows how the flame profile changes if Φ_D is held constant and $v_o d^2/D_o$ is varied. Fig. 12 gives the change in flame profile for a constant value of $v_o d^2/D_o$ and three incremental values of Φ_D . The curves follow the quadratic relationship between flame height and width given by Eq. (23). The plots also show the expected trends in flame height with velocity, diffusivity, burner dimension, and fuel to air ratio. Figure 11 shows that the flame height increases with increasing velocity or fuel supply tube width and decreases with increasing diffusivity. Figure 12 shows that the flame height also increases with increasing Φ_D, which indicates that the flame lengthens as the supply fuel/oxidizer ratio increases. A look at the time for fuel consumption will show how these curves correctly reflect the influence of these variables on flame height.

If H is the height of the flame then the time for a particle at the center of the flow to travel the length of the flame is H/v_o. During this same time the oxidizer diffuses to the particle over half the width of the fuel supply tube. The diffusion time can be approximated as X_o^2/ D_o. Equating these two expressions and solving for H gives

$$H=\frac{v_o X_o^2}{D_o} \tag{42}$$

This relationship indicates that the height of the flame is increased by increasing the velocity or fuel supply tube width and decreased by increasing the diffusivity, which are

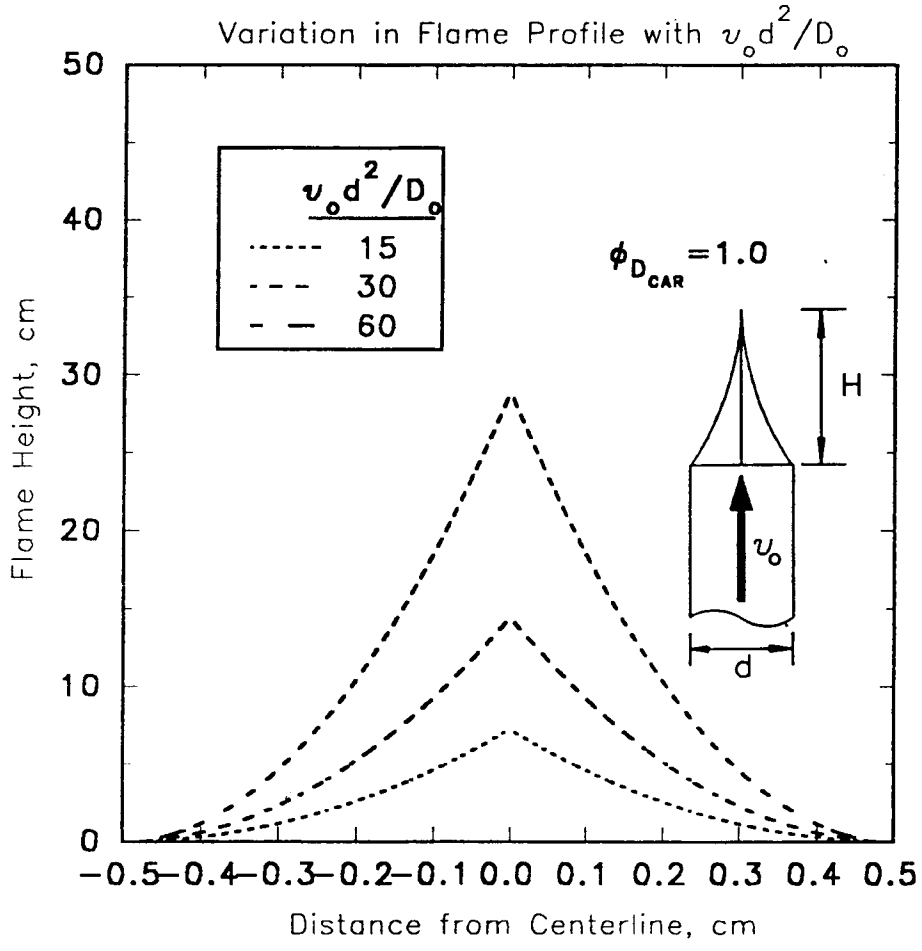

Figure 11. Flame Model Profiles: Variation with $v_o d^2/D_o$

the same effects demonstrated in Fig. 11. The increase in flame height with increasing Φ_D be explained on the basis that increasing the fuel to oxidizer supply ratio increases the amount of fuel to consume relative to the oxidizer concentration and therefore takes more time, which results in a taller flame.

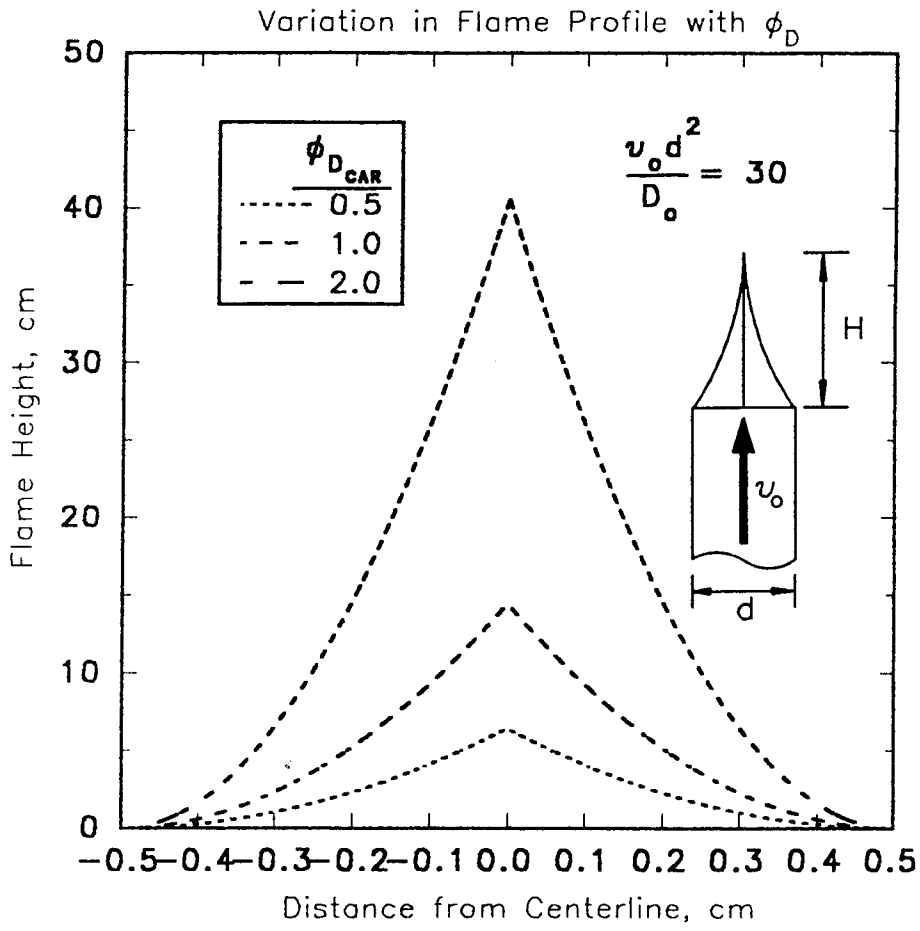

Figure 12. Flame Model Profiles: Variation with Particle to Oxidizer Ratio

Equation (42) can be used to give a dimensionless quantity

$$\frac{HD_o}{v_o d^2} = \text{constant} \tag{43}$$

where d is the supply tube width. This is essentially the information contained in Eqs. (23) and (28), which state that the similarity variable is a constant λ for a given value

of Φ_D. Equation (43) is one-sixteenth of the square of the inverse of the similarity variable evaluated at $2X_o=d$. So the information about flame height as it varies with velocity, fuel supply tube width, diffusivity, and fuel to oxidizer mass ratio should be representable in a plot of HD_o/v_od^2 versus Φ_D. Figure 13 is a plot of the dimensionless flame height HD_o/v_od^2 versus Φ_D and represents not only the axial flame height but also the entire flame profile if H is taken as the height of the profile at any thickness $d=2X$.

The quadratic profile of the particle flame model is quite different from that of a diffusion flame between gaseous fuel and oxidizer. The classic over-ventilated Burke-Schumann flame profile bulges out away from the edge of the fuel supply tube before closing at the flame tip such that the maximum width of the flame is wider than the mouth of the tube. In contrast, the maximum width of the particle flame occurs at the mouth of the fuel supply tube and is equal to the width of the mouth. This is to be expected since the particles do not expand the flame by diffusing into the oxidizer, as they do in the Burke-Schumann,1928, model.

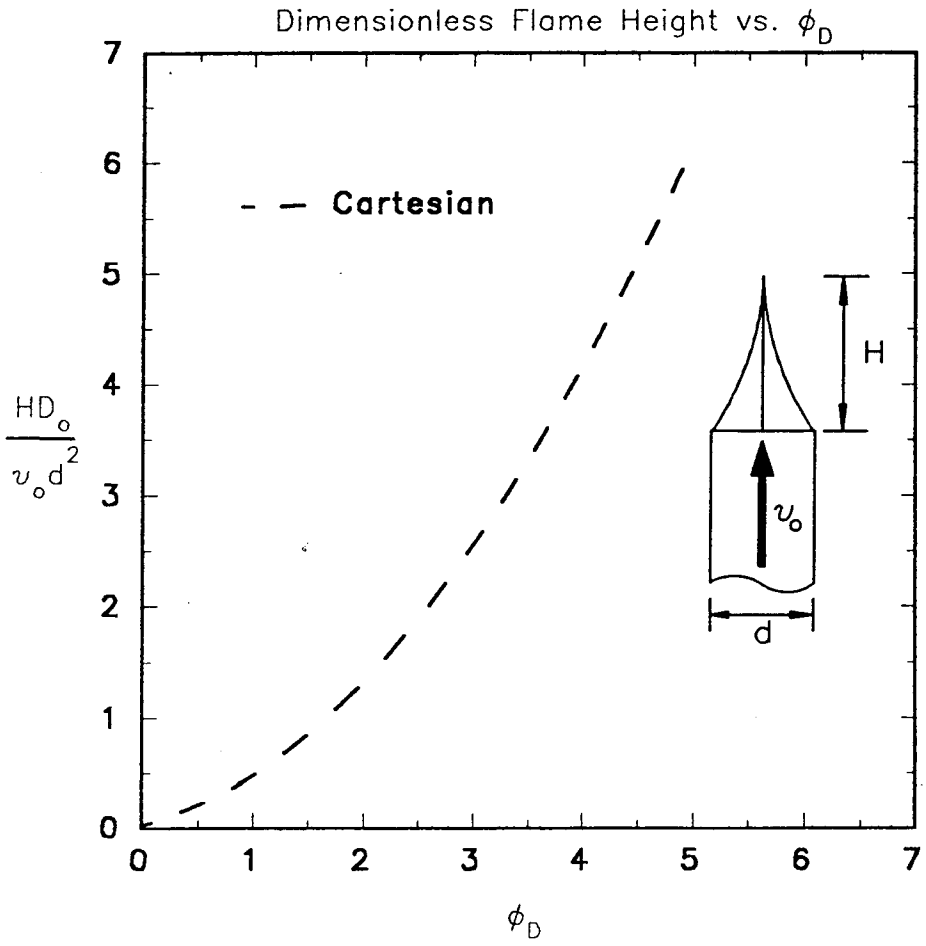

Figure 13. Dimensionless Flame Height vs. Φ_D

5. MAGNESIUM-WATER VAPOR REACTION PROFILE

The magnesium/water vapor reaction profile was measured for one flow rate of argon using digitization of high speed video of the reaction profile. Since the cylindrical model of the flame given in Chap. 4 has not been completely developed it is not possible to make a comparison between theory and experiment. However, the flame height given by Eq. (42) is a reasonable estimate and is of the same order of magnitude as the experimental results.

5.1 Experimental Procedure

The reaction profile was produced using an overall stoichiometry of 1.7 for the hydrogen/air flame. The stoichiometry was based on a comparison of hydrogen flow rates as described below. Using the same air flow rate, the hydrogen flow rate was measured for the reaction profile conditions and when the temperature near the bottom outside edge of the profile was a maximum. At this maximum temperature the stoichiometry was assumed to be approximately one. The ratio of the experimental hydrogen flow rate to the stoichiometric flow rate is the experimental stoichiometry. Using a fuel rich stoichiometry adjacent to the magnesium reaction zone ensured that the oxygen in the reactant atmosphere was completely consumed and the magnesium was reacting solely with water vapor.

In order to determine Φ_D, the ratio of supply to stoichiometric concentration ratios, the freestream concentration of the oxidizer must be determined as well as the

bulk concentration of the magnesium flow. The freestream concentration of the oxidizer for this experiment is that of the water vapor which can be determined from the flow rates of hydrogen and air.

Flow rates of 1.19×10^{-4} m^3/s and 1.67×10^{-4} m^3/s were measured for the hydrogen and air flow rates using Matheson rotameter model numbers 603 and 604, respectively. The volume flow rate of oxygen is 21% that of the air, or 3.5×10^{-5} m^3/s. Note that under the conditions of the experiment the gases could be considered ideal. Written as a rate equation the ideal gas law becomes $P\dot{V} = \dot{n}\bar{R}T$, where $\dot{V}$ is the volume flow rate and $\dot{n}$ is the molar flow rate. Since P, $\bar{R}$ and T are the same for all the gases their volume flow rates are proportional to their molar flow rates. This means that for complete combustion of the oxygen the flow rate of water vapor is two times the flow rate of oxygen and the flow rate of water vapor plus the flow rate of hydrogen in the products is the same as the supply flow rate of hydrogen. The mole fraction of water vapor in the products is the percent volume flow rate of water vapor of the total flow rate, or $X_{H2O} = 2(0.35)/((0.79)1.67 + 1.19) = 0.28$. Using the ideal gas law as applied to partial concentrations gives the freestream concentration of the water vapor as the product of the mole fraction and the total concentration

$$C_{H2O} = \frac{X_{H2O} P}{\bar{R} T} \tag{44}$$

For a pressure of one atmosphere and an average freestream temperature of 1400 K, $C_{H2O} = 2.44$ mole/m^3.

The density of the magnesium is the mass flow rate of magnesium divided by the argon volume flow rate. However, both flow rates are changing over the time of the experiment. As the density of the magnesium increases in the particle formation chamber the mass flow rate of magnesium and the temperature of the flow increase. By the ideal gas law, the volume flow rate of argon increases in proportion to the temperature. Since both flow rates increase, the change in the magnesium density over the life of the experiment is minimized.

As mentioned in Chap. 2, the magnesium flow was stable for about two minutes. The profile was measured during the latter part of the second minute, so the flow rates of magnesium and argon correspond to average values for the latter half of the experimental time frame.

An argon volume flow rate of 2.2×10^{-5} m^3/s was measured with a Matheson model #604 rotameter. The temperature of the flow at the outlet was approximately 10 percent greater than the temperature at the rotameter. Adjusted for this temperature change the volume flow rate becomes 2.42×10^{-5} m^3/s. The mass flow rate of magnesium of approximately 1.3 mg/s was determined by collecting and weighing the magnesium for the second minute of stable flow. The magnesium was produced with the particle formation chamber operating under experimental conditions, but without a magnesium/water vapor reaction present, and drawn into filter paper using suction. Weighing the filter paper before and after the collection gave the mass of magnesium. The mass flow rate of the magnesium is the quotient of the mass collected and the time for collection.

The magnesium mass flow rate and the argon volume flow rate gave a magnesium bulk density of 53.7 g/m^3. Dividing by the molecular weight of magnesium gave the concentration as 2.21 mole/m^3. Measurements of the flow rate for the last 30 seconds of the stable flow indicated that the average flow rates for the second half and the whole of the collection period did not differ by more than 20 percent. The corresponding variation in the argon volume flow rate was approximately 10 percent yielding an error of $\pm$ 10 percent for the density.

The ratio of the magnesium concentration to the water vapor concentration gives f_{supp}=0.906. The water and magnesium are assumed to react according to

$$Mg+H_2O=MgO+H_2 \qquad (45)$$

Since one mole of magnesium reacts with one mole of water vapor, the stoichiometric ratio f_{st} is one. The ratio of f_{supp} to f_{st} is Φ_D which is approximately 0.9 for this experiment.

The velocity of the argon is the volume flow rate divided by the cross-sectional area of the transport tube. For an inside diameter of 7 mm the velocity is approximately 60 cm/s. The diffusion coefficient for water vapor in nitrogen was determined to be approximately 3 cm^2/s using an empirical correlation given by Cussler, 1984,

$$D_o=\frac{1x10^{-3}T^{1.75}(1/M_1+1/M_2)^{1/2}}{P[(\sum V_{i1})^{1/3}+(\sum V_{i2})^{1/3}]^2} \qquad (46)$$

evaluated at an average temperature of 1400 K for the hydrogen/air flame. In Eq. (46) T is the absolute temperature, M_1 and M_2 are the molecular weights of the two species,

P is the pressure in atmospheres, and the V_{ij} are the volumes of the parts of the molecule j. For nitrogen and water the ΣV_{ij} are 17.9 and 12.7, respectively.

5.2 Reaction Profile Appearance

The reaction profiles in Figs. 14 (a)-(d) are video frames showing the change in the reaction profile as the magnesium flow rate increases. Figure 14(a) shows the profile shortly after the magnesium flow has been established, 14(b) is near the middle of the experiment, and Figs. 14(c) and 14(d) are sequential frames near the end of the stable flow. The shutter speeds for Figs. 14(a), 14(b), and 14(c) and (d) were 1/60, 1/500, and 1/1000 s, respectively. With these shutter speeds only Fig. 14(a) appears the same as viewed with the naked eye. While distorting the visual appearance, increasing the shutter speed gave a more defined outline for measurement of the reaction profile.

The reaction profile is bullet-shaped and appears as a yellow-orange color. Spectrograph wavelength measurements indicate that the yellow is emission from sodium contaminants in the hydrogen/air flame. The top and bottom of the reaction profile is blurred and gives a strong white glow. The edges of the mid-section of the profile are bright and distinct but the region between the edges is pale. As the flow rate of magnesium increased the size and brightness of the blurred regions also increased, but this effect is diminished by the higher shutter speeds used for Figs. 14(b), 14(c), and 14(d). The differences in the appearance of the profile are explained in detail in Chap. 6. Note that the reaction appears to start about 3 mm above the outlet of the tube on the right side but begins at about twice this height on the left side. This unevenness is due

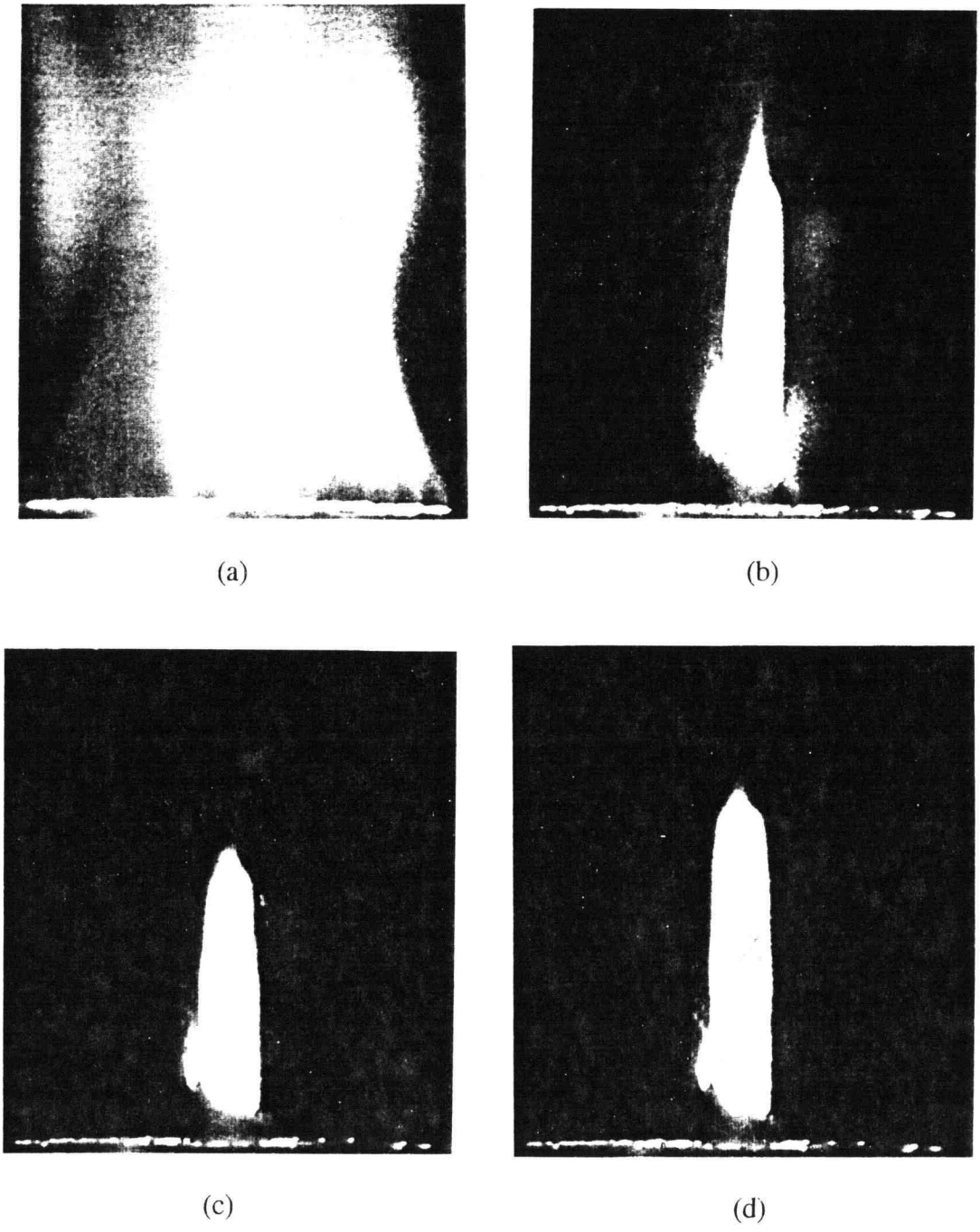

Figure 14. Experimental Magnesium/Water Vapor Reaction Profiles

to poor distribution of air flow around the supply tube which causes variation in the location of the product zone of the hydrogen/air flames. These product zones are most visible in Fig. 14(a) as bright, V-shaped patterns below and on either side of the magnesium reaction zone. The beginning of the magnesium reaction profile appears to correspond to the hot product region at the end of the hydrogen/air flames. At the bottom of the flame what appeared to be individual particle traces could be seen flowing up from the reaction zone. These particles can be seen in the left side of Figs. 14(b), (c), and (d).

The two flames shown in Fig. 15 are two sequential video frames showing the instability in the magnesium flow alluded to in Chap. 2. Obviously, these large variations in the flow rendered measurements difficult. The fluctuations started small and grew to the point that the arc was extinguished. After extinguishment a stable and decreasing flow of magnesium was reestablished as the remaining particles were drawn from the particle formation chamber.

5.3 Results

The measured profile for the experimental conditions shown in Fig. 16 was obtained by digitizing a picture of the reaction profile from the video and measuring the contour of the digitized profile. The frame that was digitized was taken near the end of the stable flow with a shutter speed of 1/1000 s. The magnesium flow varied during this portion of the experiment, which is indicated by the change in the height of the profiles in Figs. 14(c) and 14(d), so the measured profile represents an average height.

Equation (42) gives an estimate of the reaction profile height as $r^2 v_o/D_o$, where r is the radius of the supply tube. For the experimental conditions, this estimate is 2.5 cm which is 25 percent greater than the measured height of 2 cm.

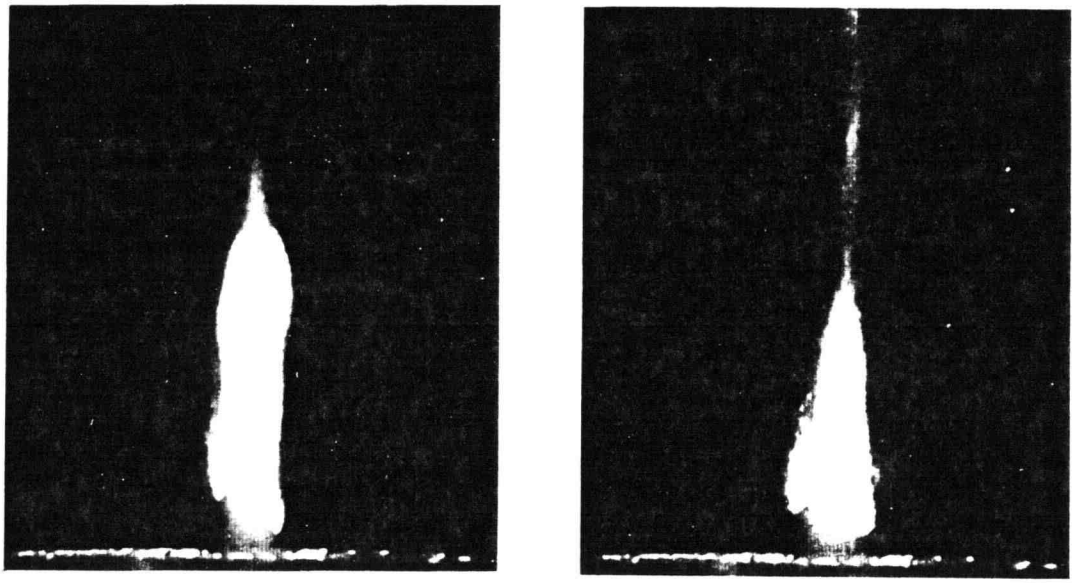

Figure 15. Sequence of Video Frames Showing Instability of Reaction Profile

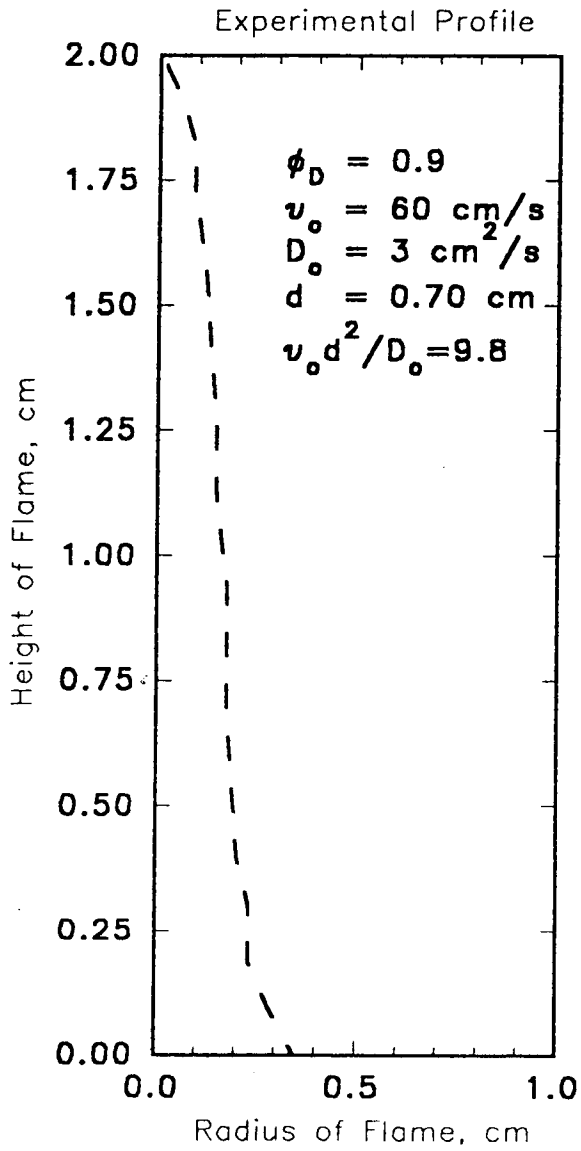

Figure 16. Measured Profile of Magnesium/Water Vapor Reaction

6. MAGNESIUM-WATER VAPOR TEMPERATURE PROFILE

In the study of diffusion-limited processes it is of interest to measure the thermal environment created by the fuel/oxidizer reaction. Temperature measurements on either side of the reaction zone can reveal information about the rate of heat release during combustion. In the case of particle reactions the rate of heat release will correlate with the oxidation rate and can be used to determine if the combustion is complete.

To determine the thermal environment created by the magnesium/water vapor reaction, thermocouple measurements were made on either side of the reaction profile location with and without particle flow. Although thermodynamic calculations indicate that the reaction of magnesium with water vapor is exothermic, the measurements indicate no change in the temperature profile with the presence of the particles. The absence of heat release suggests certain possibilities for the ignition and oxidation of the particles.

6.1 Experimental Procedure

The temperature measurements were obtained with the apparatus described in Chap. 3. The thermocouple, a type S (Pt.-Pt.10%Rh.) with a 0.127 mm wire diameter, was sheathed in double-holed high temperature ceramic tubing secured to a translation stage positionable to the nearest 25 μm. A total of one centimeter of lead length was exposed to the flame environment. The ceramic tubing was positioned horizontally, but the lead wires were bent 90 degrees at the end of the tubing so that the leads were

vertical and directed upstream into the flow. A vertical orientation was selected because the streamwise temperature gradients were very mild compared to the crossflow direction.

A temperature profile was generated at a distance approximately 1 cm above the top of the burner. This corresponds to a position within the long mid-section of the reaction profile and a profile radius of 3.2 mm. Fourteen equally spaced measurements were taken along a horizontal line approximately 8 mm long. The measurements started at a radius of 2 mm from the center of the transport tube. Temperatures were determined at similar locations with and without the magnesium/water vapor reaction present.

For some measurements with the reaction present the thermocouple became coated with what appeared to be magnesium oxide, causing the temperature readings to drop. A correction was obtained for these measurements by determining the temperature at several points out of the product flow with the thermocouple both bare and coated. The average of the differences between the coated and uncoated readings gave the correction.

6.2 Temperature Profile

The thermocouple model introduced in Chap. 3 was used to obtain the true temperature of the environment. The model accounts for the radiation to the ambient surroundings, the conduction in the lead wires, and the convection with the surrounding hot environment for the bead and lead wires. The conduction in the leads is affected by the temperature of the environment around the leads. Therefore, an accurate determination of the gas temperature at the bead must include the environment

temperature around the leads.

In order to obtain the gas temperature along the leads nine equally spaced measurements were taken in a vertical line over a length of 1 cm. The lowest point in this line of measurements was the point one centimeter above the top of the burner. The other eight measurements were used to determine the temperature profile for the leads. The first temperature determined was the temperature at the highest location. Although the environment around the leads was not known for this measurement it was approximated using the pattern of the last two or three readings in the vertical line of measurements. The next temperature in the vertical line was found using the temperature at the highest location and the approximated profile beyond the highest point. The procedure continued this way with each temperature in the vertical line being determined with a lead profile that consisted of the environment temperatures already found and a portion of the approximated profile. As each temperature is determined, more of the temperatures generated by the model and less of the approximated profile is used for the lead environment. The temperature at the lowest point is determined using a lead profile that consists entirely of temperatures obtained using the model.

For the temperatures determined for the lowest point of one centimeter above the burner, the accuracy of the temperatures obtained for the top of the lead environment are affected by the use of the approximated profile. However, the influence of the approximated profile is diminished by the fact that the modeled bead temperature is insensitive to large changes in the temperature of the lead profile farthest from the bead. A change of 50 K in any of the last four temperatures of the lead profile caused a

maximum deviation in the bead temperature of 1 K. This insensitivity to temperatures in the lead profile that are the least accurate coupled with the fact that the gradient in the vertical direction is very mild gives confidence to the accuracy of the temperatures obtained using the thermocouple model.

The results of the reaction profile measurements are given in Fig. 17. The profile first increases, peaks at a radius that is 2 mm greater than the radius of the magnesium/water vapor reaction, and then decreases as the radius increases. Only one curve is given because the temperature measurements were the same whether or not the particles were present. This unchanging temperature profile is not limited to the mid-section of the reaction zone, however, as the same result was found at the top and bottom of the reaction profile when they were probed with a thermocouple. Although the reaction of magnesium with water vapor is exothermic, the fact that the temperature does not change when the particle flow is introduced indicates that negligible heat is released from the magnesium/water vapor reaction to the surrounding gas. Examination of the appearance of the flame and the ignition temperature and heat generation of the particles lend support to this conclusion.

6.3 Magnesium Oxidation

As mentioned in Chap. 5, the reaction zone can be separated by appearance. Since the top and bottom of the profile are distinct from the long mid-section they will be considered separately.

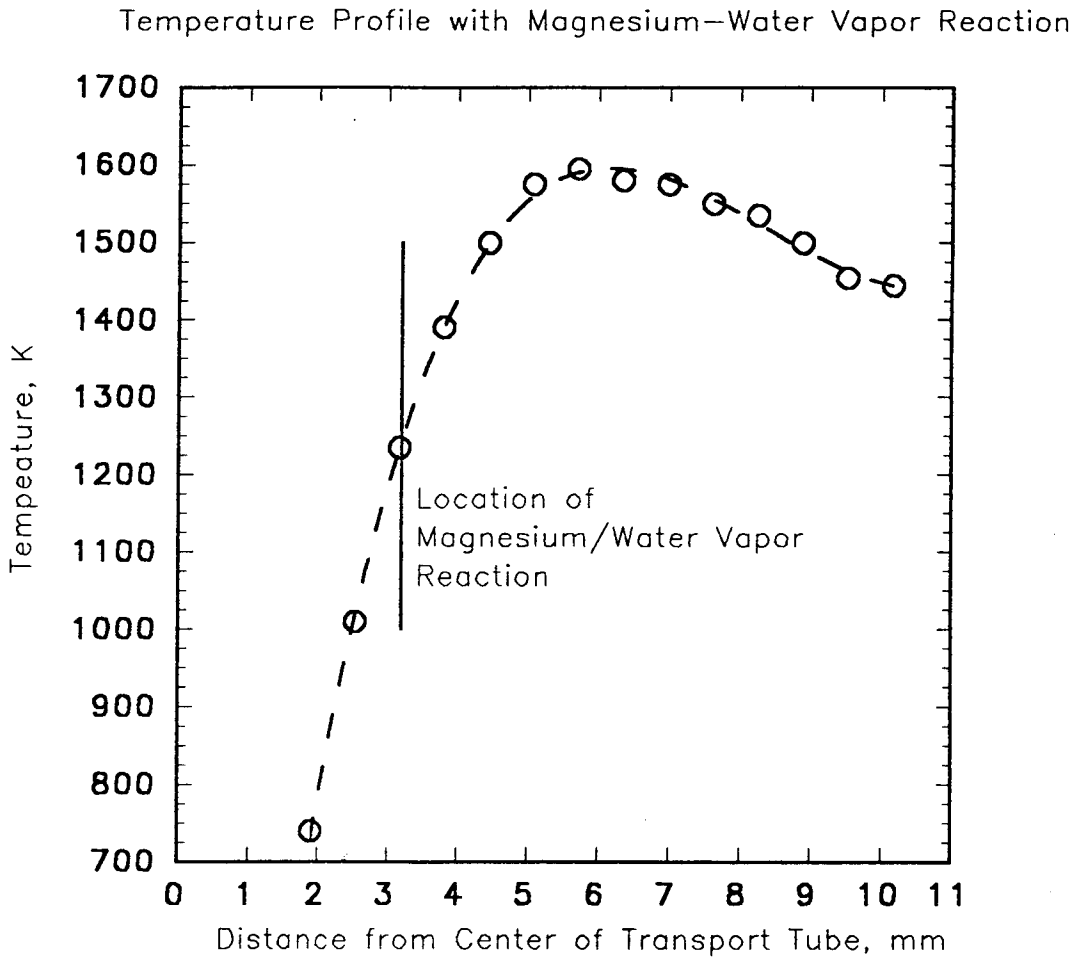

Figure 17. Temperature Profile with Magnesium/Water Vapor Reaction

The mid-section of the reaction zone is pale yellow-orange with a stronger whiteglow along its edge. The bright edge appearance is presumably do to viewing more radiation from the thicker portion of the profile along its curvature. Although the heat of reaction of water vapor and magnesium is about half that of magnesium and oxygen it is expected that the water vapor reaction will give off the same familiar white glow of the latter reaction but with less intensity. Since the mid-section does not give off the

bright radiation of an exothermic reaction it is possible that the particles are not igniting and their faint glow is due to surface reactions. The distinct outline of the mid-section is also characteristic of particle surface reactions (Gordon, 1960).

Ignition will occur if the heat gained from the oxidation reactions at the particle surface outweighs the losses due to convection and radiation such that the temperature rise of the particle continues at an accelerating rate (Markstein, 1963). The temperature of the environment when ignition occurs is referred to as the ignition temperature. Ignition is followed by rapid oxidation of the particle. If the particle does not ignite oxidation will still occur, but at a slower rate and it may be incomplete.

Most of the studies of the ignition temperature of magnesium particles have used air or oxygen as the reactive atmosphere and those studies that have investigated water vapor as a reactant have only considered it as an additive to air (Coffin, 1955; Markstein, 1963). Nonetheless, information about the ignition temperature of magnesium in water vapor can be inferred from the studies with oxygen. Cassel and Liebman, 1959, measured the ignition temperature of individual magnesium particles. Their findings are reproduced in Fig. 18. The curve has been extrapolated to the one micron size of particle used in this study and the temperature for this diameter is approximately 900 °C or 1170 K. It is reasonable to assume that the ignition temperature in water vapor will be greater since the heat of reaction is much less than that for oxygen. Figure 17 shows the temperature at the reaction zone to be approximately 1250 K. It is possible that the ignition temperature is greater than 1250 K and the particles along the mid-section do not ignite. If this is true then heat would still be generated by reactions on the particle

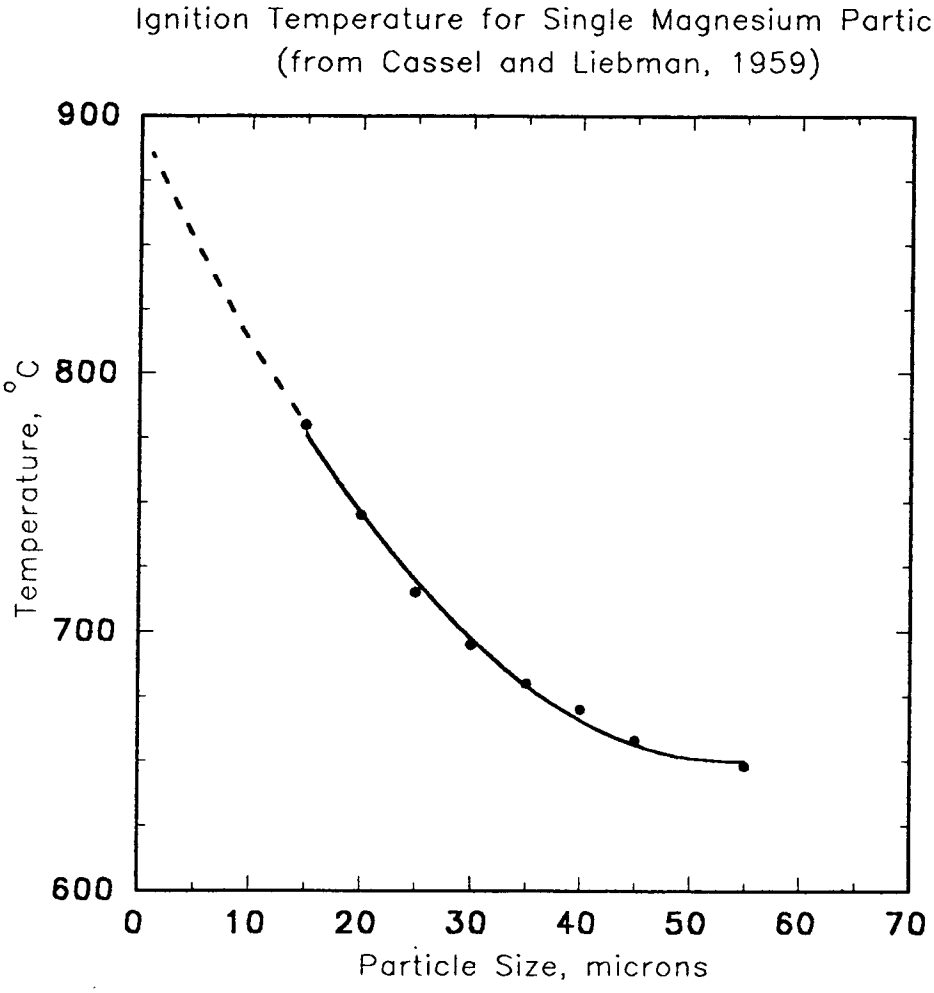

Figure 18. Ignition Temperature for Single Magnesium Particles (from Cassel and Liebman, 1959)

surface but at a much slower rate and most of it would be absorbed by the remaining unburned magnesium. Consequently, the temperature in the surrounding gases would not be affected.

The brighter glow from the particles at the top and bottom of the reaction profile

indicates ignition has occurred. This conclusion is also supported by the streaks of light that can be seen issuing from the bottom of the reaction zone. These are most likely particles that have ignited and continue to burn as they leave the initial reaction zone. The temperature measurements at these two zones indicate that they are at least 100 K greater than the temperature along the midsection. The higher temperature may be enough to ignite the particles.

The appearance of the top and bottom of the reaction zone is also consistent with the mode of combustion for magnesium which has been observed to undergo what is known as vapor-phase burning (Coffin, 1955). Magnesium is vaporized from the particle surface and burns in a shell around the particle. This gives the particle a blurred appearance, and a continuous flow of burning particles could create the fuzzy outline of the top and bottom of the reaction zone. It was observed with high speed video that the glow at the bottom of the flame is in fact due to individual particles that can not be distinguished with the naked eye.

Although these particles do appear to ignite the distributed nature of their burning and the loss of heat by radiation may make the heat loss to the surrounding gases undetectable. Figure 14(a) shows that the magnesium starts to burn at the ends of the hydrogen/air flames adjacent to the particle flow, where the environment will be hottest. At this location the particles can be seen to burn over a short distance, which means the heat they release is also distributed over this length. This distributed burning is also compounded by the fact that the oxidation is separated into two regions, which hinders the concentration of any energy released during combustion.

In addition, a significant portion of the energy generated by combustion may not be transferred to the surrounding gases. When the magnesium burns the hot product formed is magnesium oxide liquid because the heat of reaction is not sufficient to overcome the heat of vaporization. This conclusion is supported by measurements of the burning temperature of magnesium in air that found the upper limit to be the vaporization temperature of magnesium oxide (Wolfhard and Parker, 1949; Glassman, 1960; Markstein, 1963). The hot oxide droplets become solid particles as they cool to the temperature of the reactive atmosphere by convection and radiation heat transfer. Most of the energy lost during cooling will be radiation because the heat loss for radiation is proportional to the temperature of the particles to the fourth power whereas it is proportional to the temperature to the first power for convective heat transfer. Furthermore, the particles radiate to the cool surroundings at room temperature while they convect heat to the hot reactive atmosphere. Therefore, any heat transfer to the reactive atmosphere from the particles would be the convected portion of their total energy of combustion.

Given the distributed and radiative mode of energy release for the particles, it seems likely that the change in the surrounding gas temperature would be small at best. Unfortunately, the method used to measure the temperature change would not be able to detect small variations in the thermal environment because the build up of oxide on the thermocouple diminished its sensitivity.

7. CONCLUSION

7.1 Accomplishments

A diffusionally controlled reactive synthesis process has been studied. A reaction between water vapor and a magnesium particle stream was created by moving a particle laden flow into a hot atmosphere of nitrogen, hydrogen, and water vapor. A multi-tube diffusion burner was developed to produce the hot atmosphere. The thermal characterization of this burner showed individual diffusion flames that were distinctive near the outlet of the tubes but blended together to form a uniform thermal environment within 1 cm over the tubes.

A flame profile model was developed for a particle stream reacting with an oxidizer in parallel flow. A key assumption of the model is the absence of any particle diffusion. The resulting model, based on a stoichiometric fuel/oxidizer balance at the flame surface and the conservation of the oxidizer species, gives a quadratic relationship between flame width and height for cartesian coordinates.

7.2 Further Study

Since this is the first study of a diffusionally controlled particle stream/oxidizer reaction the opportunities for continued study are abundant. First, the exploration of a hotter oxidizing environment could prove to give more satisfactory results between model and results simply because the particles may oxidize more rapidly. A hydrogen/oxygen flame would provide this hot reactive atmosphere.

Second, other metals besides magnesium could be investigated and the method of particle formation improved. To be viable, this synthesis process should be able to produce some of the more desirable ceramics like aluminum nitride. The method of particle formation needs to work on all types of metals and have the potential to be continuous.

Along with the need to improve the method of particle formation is the need for a more uniform oxidation environment. The overall design of the burner is sound, but improvements need to be made in its method of construction.

The model is simplistic and could be improved in sophistication. The energy equation could be included in the model as well as some mechanism for describing the particle oxidation process. Also, the issues of the cylindrical coordinate system need to be resolved.

Combustion synthesis is an exciting field of study and this work takes the initial step in the exploration of a new method of ceramic production using reaction synthesis.

BIBLIOGRAPHY

Bauer, J., Biste, L., and Bolze D., 1977, "Optical Properties of Aluminum Nitride Prepared by Chemical and Plasmachemical Vapor Deposition", Phys. Stat. Sol. (a), Vol. 39, pp. 173-181

Beck, A., (Ed.), 1940, The Technology of Magnesium and its Alloys, 1940, F.A. Hughes and Co., London, pp. 482

Benedict, R.P., (Ed.), 1981, Manual on the Use of Thermocouples in Temperature Measurements, ASTM STP470B, American Society for Testing and Materials, pp. 26,27,41

Brzustowski, T.A., and Glassman, I., 1964, "Vapor-Phase Diffusion Flames in the Combustion of Magnesium and Aluminum I. Analytical Developments; II. Experimental Observations, in Progress in Astronautics and Aeronautics, (Wolfhard, H.G., Glassman, I., and Green, L., Eds.), Academic Press, New York, Vol. 15, pp 75-158

Burke, S.P., and Schumann, T.E, 1928, "Diffusion Flames", Industrial and Engineering Chemistry, Vol. 20, pp. 998-1004

Carslaw, H.S., and Jaegar, J.C., 1959, Conduction Heat Transfer, 2nd. Ed., Oxford University Press, New York

Cassel, H. M., and Liebman, I., 1959, "The cooperative mechanism in the ignition of dust dispersions," Combust. Flame, Vol. 3, pp 467-475

Coffin, K.P., 1955, "Some physical aspects of the combustion of magnesium ribbons," Fifth Symposium International on Combustion, Reinhold Publishing Corp., New York, pp. 267-276

Cussler, E. L., 1984, DIFFUSION: Mass transfer in fluid systems, Cambridge University Press, Cambridge

Demiryont, H., Thompson, L.R., and Collins, G.J., 1986, "Optical and electrical characterizations of laser-chemical-vapor-deposited aluminum oxynitride films", J. Appl. Phys, Vol. 59, pp 3235-3240

Elliot, D.J., 1986, Microlithography Process Technology for IC Fabrication, McGraw-Hill, New York, pp. 358-359

Fassell, W.M., Papp, C.A., Hildenbrand, D.L., and Sernka, R.P., 1960, "The Experimental Nature of the Combustion of Mettalic Powders", in Progress in Astronautics and Rocketry, (M. Summerfield, Ed.), Academic Press, New York, Vol. 1, pp. 259-269

Fristrom, R.M. and Westenberg, A.A., 1965, Flame Structure, McGraw-Hill, New York, pp 103-110

Glassman, I., 1960, "Combustion of Metals: Physical Considerations," in Progress in Astronautics and Rocketry, (M. Summerfield, Ed.), Academic Press, New York, Vol. 1, pp.253-257

Gordon, D. A., 1960, "Combustion characteristics of metal particles," in Solid Propellant Rocket Research, Academic Press, New York, pp. 271-278

Hencken, K. R., 1994, personal communication.

Hlavacek, V., 1991, "Combustion Synthesis: A Historical Perspective", Ceramic Bulletin, Vol. 70, pp. 240-243

Karlekar, B.V., and Desmond, R.M., 1982, heat transfer, Second Edition, West Publishing Company, St. Paul, pp. 776

Kashireninov, O. E., 1990, "Metals vapour oxidation in diffusion flames", Pure & Appl. Chem., Vol. 62, pp. 851-859

Krupa, R.J., Zizak, G., and Wineforder, J.D., 1986, " Shielded flashback-resistant diffusion flame burner for combustion diagnostics", Applied Optics, Vol. 25 pp. 3600-3601

Law, C. K., 1973, "A Simplified Theoretical Model for the Vapor-phase Combustion of Metal Particles", Combustion, Science and Technology, Vol. 7, pp 197-212

Markstein, G.H., 1963, "Combustion of Metals", AIAA Journal, Vol. 1, pp. 550-562

Markstein, G.H., 1964, "Analysis of a Dilute Diffusion Flame Maintained by Heterogeneous Reaction," in Progress in Astronautics and Aeronautics, (Wolfhard, H.G., Glassman, I., and Green, L., Eds.), Academic Press, New York, Vol. 15, pp 177-202

Meikle, S., Nomura, H., Nakanishi, Y., and Hatanaka, Y., "Reactions of atomic nitrogen and trimethyl aluminum downstream from a nitrogen microwave

plasma", J. Appl. Phys., Vol. 67, pp. 483-486

Miyamoto, Y., 1990, "New Ceramic Processing Approaches Using Combustion Synthesis Under Gas Pressure", Ceramic Bulletin, Vol. 69, pp. 686-690

Nakai, S. and Okazaki, T., 1975, "Heat Transfer from a Horizontal Circular Wire at Small Reynolds and Grashof Numbers - II", Int. J. Heat Mass Transfer, Vol.18, pp. 397-413

Nickel, K.G., Riedel, R., and Petzow, G., 1989, "Thermodynamic and Experimental Study of High-Purity Aluminum Nitride Formation from Aluminum Chloride by Chemical Vapor Deposition", J. Am. Ceram. Soc., Vol 72, pp. 1804-10

OMEGA ENGINEERING, INC., 1992, OMEGA Complete Temperature Measurement Handbook and Encyclopedia, Vol. 28, OMEGA ENGINEERING, INC., Stamford, CT, pp. Z-172

Roper, F.G., 1977a, "The Prediction of Laminar Jet Diffusion Flame Sizes: Part I. Theoretical Model", Combust. Flame Vol. 29, pp. 219-226

Roper, F.G., Smith, C., and Cunningham, A.C., 1977b, "The Prediction of Laminar Jet Diffusion Flame Sizes: Part II. Experimental Verification", Combust. Flame Vol. 29, pp. 227-234

Roper, F.G., 1979, "Laminar Diffusion Flame Sizes for Interacting Burners", Combust. Flame, Vol. 34, pp. 19-27

Schrenk, W.G., 1986, "Historical Development of Flame Excitation Sources for Analytical Spectroscopy", Appl. Spectrosc., Vol. 40, pp xix-xxviii

Shaffer, P.T.B., Schorr, J.R., and Hexemer, R.L., 1989, "Green Light to Aluminum Nitride", Ceramic Industry, Vol. 132, no. 5, pp. 25-27

Sohn, H.Y. and Harbuck, D.D., 1986, "Aluminum from Coal Wastes through the formation of Aluminum Nitride by Carbothermal Reduction under Nitrogen", Ind. Eng. Chem. Prod. Res. Dev., Vol. 25, pp. 367-372

Weast, R.C., (Ed.), 1970, Handbook of Chemistry and Physics, Fifty-first Edition, The Chemical Rubber Company, Cleveland, Ohio, pp. E10

Welty, J.R., Wicks, C.E., and Wilson, R.E., 1969, Fundamentals of Momentum, Heat, and Mass Transfer, John Wiley and Sons, New York, pp. 354

Wolfhard, H.G., and Parker, W.G., 1949, "Temperature measurements of

flames containing incandescent particles," Proc. Phys. Soc. (London) 62B, pp. 523-529

Yoshida, S., Misawa, S., and Itoh, A., 1975, "Epitaxial growth of aluminum nitride films on Sapphire by reactive evaporation", Appl. Phys. Lett., Vol. 26, pp. 461-462

Yoshida, S., Misawa, S., Fujii, Y., Takada, S., Hayakawa, H., Gonda, S., and Itoh, A., 1979, "Reactive molecular beam epitaxy of aluminum nitride", J. Vac. Sci. Technol., Vol. 16, pp. 990-993

APPENDIX

The FORTRAN code listed below is one version of the program used to determine the true environment temperature from the measured temperatures. Several versions of this program were created to allow different levels of user interaction and to model all of the different environments measured. Version 5A shown here and version 6 allow the user to input more of the variables that effect the solution, whereas the rest of the versions have some of these variables hardcoded to match the system and the chosen solution parameters.

Versions 5A and 5B model the situation when the short leg of the thermocouple, Fig. 3 in Chap. 3, is above the center of the concentric circles in Fig. 4 of Chap. 3. Version 5C is for the measurements made with the short leg below the center of the concentric circles. Versions 6 and 7 are used to model the environment when the thermocouple is straight and placed between the rows of tubes. Version 8 was created for the reaction profile temperature measurements.

```
*******************************************************
* PROGRAM TO CALCULATE THE HEAT LOSSES THROUGH THE  *
* LEAD WIRES OF A THERMOCOUPLE, TAKING INTO ACCOUNT *
* THE RADIATIVE AND CONVECTIVE HEAT TRANSFER FROM   *
* THE WIRE AND THE CONDUCTION DOWN THE WIRE         *
*******************************************************
C
      PROGRAM TCBEAD5A   !VERSION 5A - DETERMINE TEMP PROFILE OVER TUBES
      DOUBLE PRECISION T(-1:500),ERROK,ERR,ERRMAX,TOLD,TS,PI,SIGMA,DTDX,
     :TMAX(1:10),TINF(-1:531),EPS,KAIR,H,A,B,DX,DBEAD,DWIRE,RM(0:20),
     :ABEAD,AWIRE,COND,CONV,RAD,WIRESEG,WIREL,DTDXEND,TISOTHRM(-1:20),
     :RO,DYTOTAL,DY(0:20),DR,TMIN(0:10),KTC
C
C  ECHO VERSION OF PROGRAM
C
      PRINT*,'TCBEAD5A - VERSION 5A - DETERMINE TEMP PROFILE OVER TUBES'
      PRINT*
C
C DATA INPUT SECTION
```

```
C
      PRINT*,'ENTER THE VALUE OF THE RADIUS, R, (M) '
      READ*,RO
      PRINT*,'ENTER THE VALUE OF DELTA-R (M) '
      READ*,DR
      PRINT*,'ENTER THE NUMBER OF ISOTHERMS '
      READ*,NISOTHRM
      NISOTHRM=NISOTHRM-1
      DO 1 I=0,NISOTHRM
         PRINT*,'ENTER THE TEMP. (K) OF ISOTHERM',I,' '
         READ*,TISOTHRM(I)
1        RM(I)=RO-I*DR
      PRINT*,'ENTER THE LENGTH OF THE WIRE (M) '
      READ*,WIREL
      PRINT*,'ENTER THE DIAMETER OF THE BEAD (M) '
      READ*,DBEAD
      PRINT*,'ENTER THE DIAMETER OF THE WIRE (M) '
      READ*,DWIRE
C     PRINT*,'ENTER MAXIMUM T INFINITY '
C     READ*,TMAX
      PRINT*,'ENTER MINIMUM T INFINITY UPPER RIGHT CORNER '
      READ*,TMIN(0)
      PRINT*,'ENTER NODE SPACING (M) '
      READ*,DX
      PRINT*,'ENTER GRADIENT AT CERAMIC '
      READ*,DTDXEND
      PRINT*,'ENTER MAXIMUM ALLOWABLE ERROR '
      READ*,ERROK
      PRINT*,'ENTER THE RELAXATION FACTOR '
      READ*,RELAX
C
      DATA PI,SIGMA,TS /3.14159,5.67D-8,300.0D0/
C
C CALCULATE STARTING TEMPERATURE PROFILE
C
      DO 2 I=-1,500
         T(I)=0.0D0
2        TINF(I)=0.0D0
      WIREL=WIREL-(DBEAD+RO+RM(NISOTHRM))
      WIRESEG=0.00160D0
      NUMSEGS=WIREL/WIRESEG
      DO 21 I=1,NUMSEGS/2+1
          PRINT*,'ENTER TMAX ',I,' '
          READ*,TMAX(I)
          PRINT*,'ENTER TMIN ',I,' '
21        READ*,TMIN(I)
      NWIRESEG=IDNINT(WIRESEG/DX)
      NTOTAL=NUMSEGS*NWIRESEG+IDNINT((RO+RM(NISOTHRM))/DX)
      IF (NTOTAL.GT.499) THEN
         PRINT*,'MORE THAN 499 NODES, CHANGE ARRAY SIZE'
         GO TO 999
```

```
      ENDIF
      DYTOTAL=0.0D0
      DO 3 I=NISOTHRM,1,-1
        DY(I)=(RM(I-1)**2-RM(NISOTHRM)**2)**.5-DYTOTAL
3       DYTOTAL=DYTOTAL+DY(I)
      DY(0)=RO-DYTOTAL
      TISOTHRM(-1)=TMAX(1)-(RM(NISOTHRM)/RO)*(TMAX(1)-TMIN(0))
      INDEX=0
      DO 5 I=NISOTHRM,0,-1
        IF (DY(I).GT.0.0D0) THEN
          NUMNODES=IDNINT(DY(I)/DX)
          DO 4 K=0,NUMNODES
4           TINF(INDEX+K)=TISOTHRM(I)-(K*DX/DY(I))*(TISOTHRM(I)
     :                    -TISOTHRM(I-1))
        ENDIF
5       INDEX=INDEX+NUMNODES
      INDEX=IDNINT(RO/DX)
      IF (RM(NISOTHRM).GT.0.0D0) THEN
        NODESGRD=IDNINT(RM(NISOTHRM)/DX)
        DO 6 I=0,NODESGRD
6         TINF(INDEX+I)=TISOTHRM(-1)+(I*DX/RM(NISOTHRM))*(TMAX(1)
     :                  -TISOTHRM(-1))
      ENDIF
      INDEX=IDNINT((RO+RM(NISOTHRM))/DX)
      PRINT*,'INDEX = ',INDEX
      DO 8  I=1,NUMSEGS/2
        DO 7 K=0,NWIRESEG
          NODE=INDEX+K+(I-1)*2*NWIRESEG
          TINF(NODE)=TMAX(I)-(K*DX/WIRESEG)*(TMAX(I)-TMIN(I))
          NODE=INDEX+I*2*NWIRESEG-K
          TINF(NODE)=TMAX(I+1)-(K*DX/WIRESEG)*(TMAX(I+1)-TMIN(I))
7       CONTINUE
8       CONTINUE
      DO 10 I=0,NTOTAL
        IF (TINF(I).EQ.0.0D0) THEN
          TINF(I)=(TINF(I-1)+TINF(I+1))/2.0D0
        ENDIF
        IF (I.LE.20) THEN
          N=I+21
          PRINT*,I,TINF(I),N,TINF(N)
        ENDIF
10      T(I)=TMAX(1)-(I*DX/WIREL)*(TMAX(1)-TMIN(NUMSEGS/2))
      NBEAD=DBEAD/DX
      DO 11 I=1,NBEAD
11      TINF(0)=TINF(I)+TINF(0)
      TINF(0)=TINF(0)/(NBEAD+1)
C
C ITERATE ON ANSWER
C
      AWIRE=(PI*DWIRE**2)/4.0D0
      ABEAD=PI*DBEAD**2
```

```
      ITER=0
      T(NTOTAL+1)=DX*DTDXEND+T(NTOTAL)
20    ITER=ITER+1
      ERRMAX=0.0D0
      DO 30  I=0,NTOTAL+1
         CALL PROPS(T(I),TINF(I),EPS,KAIR,KTC)
         TOLD=T(I)
         IF (I.EQ.0) THEN
            H=2.0D0*KAIR/DBEAD
            T(I)=(ABEAD*DX)*(H*TINF(I)+SIGMA*EPS*TS**4)
            T(I)=T(I)+AWIRE*KTC*(4.0D0*T(1)-T(2))
            T(I)=T(I)/(DX*ABEAD*(H+SIGMA*EPS*TOLD**3)+3*AWIRE*KTC)
           ELSE
            IF (I.LE.NTOTAL) THEN
              H=1.0D0*KAIR/DWIRE
              A=4*H/KTC/DWIRE
              B=4*EPS*SIGMA/KTC/DWIRE
              T(I)=(T(I-1)+T(I+1))/(DX**2)+A*TINF(I)+B*TS**4
              T(I)=T(I)/(2/(DX**2)+A+B*TOLD**3)
             ELSE
              T(I)=T(I-1)+DTDXEND*DX
             ENDIF
           ENDIF
         ERR=ABS((TOLD-T(I))/T(I))
         IF(ERR.GT.ERRMAX)ERRMAX=ERR
         T(I)=TOLD+RELAX*(T(I)-TOLD)
30    CONTINUE
      IF (ERRMAX.GT.ERROK) GO TO 20
C
C CALCULATE ENERGY COMPONENTS AT BEAD
C
      CALL PROPS(T(0),TINF(0),EPS,KAIR,KTC)
      DTDX=(-3.0D0*T(0)+4.0D0*T(1)-T(2))/(2.0D0*DX)
      COND=-2000.0D0*KTC*AWIRE*DTDX
      CONV=(2000.0D0*KAIR/DBEAD)*ABEAD*(TINF(0)-T(0))
      RAD=1000.0D0*ABEAD*EPS*SIGMA*(T(0)**4-TS**4)
C
C  PRINT OUT RESULTS
C
      PRINT*,'ITERATIONS: ',ITER
      PRINT*
      PRINT*,'DTDX=  ',DTDX
      PRINT*,'COND=  ',COND
      PRINT*,'RAD=   ',RAD
      PRINT*,'CONV=  ',CONV
      PRINT*
      DO 100 I=0,10
100      PRINT 101,I,T(I),T(NWIRESEG+I),T(NTOTAL-10+I)
C
101   FORMAT(I5,3F11.3)
C
```

```
999   STOP
      END
C
C   SUBROUTINE TO COMPUTE EPS AND KAIR AND KTC
C
      SUBROUTINE PROPS(TTC,TAIR,EPS,KAIR,KTC)
C
      DOUBLE PRECISION TTC,TAIR,TFILM,EPS,KAIR,KTC
C
      TFILM=(TTC+TAIR)/2.0D0
      EPS=-.063450D0+.000340D0*TTC-1.944D-7*TTC**2+4.691D-11*TTC**3
      KAIR=-6.0D-4+1.0D-4*TFILM-4.5616D-8*TFILM**2+1.307D-11*TFILM**3
      KTC=77.601670D0-2.23377D-2*TTC+2.45458D-5*TTC**2-5.00651D-9*TTC**3
      RETURN
      END
```